

Acknowledgements

I would like to express my deepest gratitude to my advisor, Prof. John Sullivan for his unfailing support and patience through the entire period of my graduate study. His guidance gave this work an enhanced direction and his foresight helped achieve the many goals.

I would like to thank my parents for a lifetime love, support and continuous confidence in me. It is because of them that I am enjoying this stage of my life.

I would like to thank Praveen Kulkarni and Wei Huang, my two lab mates. Without their great help and cooperation this work could not be accomplished.

Also, I would like to thank Dr. B. Savilonis, Dr. R. Ludwig and Dr. Z. Hou for their service on my graduate committee.

I also acknowledge the help that has always been given to me with a smile by Barbara Edilberti, Barbara Furman, Pamela St. Louis and Janice Dresser, the kindest and nicest people of the Mechanical Engineering Department.

I would like to thank all the members of the CCNI Image Processing (CCIP) laboratory especially Dr. J. Zhang and Mr. Udo Benz for their constant help and support.

Finally, I would like to thank CCNI consortium and its leaders Dr. Craig Ferris, Dr. Jean King.

Summary

A common approach to segment an MRI dataset is to use a standard atlas to identify different regions of interest. Existing 2D atlases, prepared by freehand tracings of templates, are seldom complete for 3D volume segmentation. Although many of these atlases are prepared in graphics packages like *Adobe Illustrator*[®] (AI), which present the geometrical entities based on their mathematical description, the drawings are not numerically robust. This work presents an automatic conversion of graphical atlases suitable for further usage such as creation of a segmented 3D numerical atlas.

The system begins with DXF (Drawing Exchange Format) files of individual atlas drawings. The drawing entities are mostly in cubic spline format. Each segment of the spline is reduced to polylines, which reduces the complexity of data. The system merges overlapping nodes and polylines to make the database of the drawing numerically integrated, i.e. each location within the drawing is referred by only one point, each line is uniquely defined by only two nodes, etc. Numerous integrity diagnostics are performed to eliminate duplicate or overlapping lines, extraneous markers, open-ended loops, etc. Numerically intact closed loops are formed using atlas labels as seed points. These loops specify the boundary and tissue type for each area. The final results preserve the original atlas with its 1272 different neuroanatomical regions which are complete, non-overlapping, contiguous sub-areas whose boundaries are composed of unique polylines.

Table of Contents

Acknowledgements	I
Summary.....	II
Table of Contents	III
Table of Figures.....	V
1. Introduction.....	1
1.1 Medical Imaging	1
1.2 Segmentation.....	2
1.2.1 Introduction.....	2
1.2.2 Segmentation.....	3
1.3 Purpose of Research.....	6
2. Background	10
2.1 Introduction.....	10
2.2 Segmentation: Methods and Applications	10
2.2.1 Preprocessing	11
2.2.2 Feature extraction.....	14
2.2.3 Segmentation.....	17
2.2.4 Classification.....	30
2.2.5 Available tools	31
2.3 Medical Imaging Techniques.....	33
2.3.1 Introduction.....	33
2.3.2 Computerized Tomography (CT)	34
2.3.3 Magnetic resonance imaging	36
3. Rat Brain Atlas.....	43
3.1 Introduction.....	43
3.2 Swanson Rat Brain Atlas	43
3.3 Discrepancies of the atlas.....	48
3.3.1 Introduction.....	48
3.3.2 Multiple lines and curves bundled into a single boundary	49
3.3.3 Nonintersecting or over-extended spline segments	50
3.3.4 Overlapping regions.....	51
3.3.5 Remotely labeled regions.....	52
3.3.6 Other issues.....	52
4. Algorithms and results	54

4.1	Introduction.....	54
4.2	Data format	55
4.2.1	Splines.....	56
4.3	Manual Modifications.....	58
4.4	Automatic Modifications	59
4.4.1	Spline Approximation.....	59
4.4.2	Extend/Intersect/Merge.....	60
4.4.3	Identify brain regions.....	62
4.4.4	Overlapping areas	68
4.4.5	Mirroring and output.....	68
4.5	The code.....	69
4.6	Results.....	69
4.7	Conclusions.....	74
5.	References.....	77

Table of Figures

Figure 1.1: 3D reconstruction of human skull using CT images	4
Figure 1.2: Two examples of segmentation	4
Figure 1.3: Flowchart of an image analysis system	5
Figure 1.4: Application of a Segmented Atlas in a fMRI Study. T	7
Figure 2.1: RF field inhomogeneity effect	12
Figure 2.2: A noisy CT image due to low dose beam	13
Figure 2.3: Streaking artifact due to external metal objects	13
Figure 2.4: Edge Detection using Canny operator	16
Figure 2.5: General classification of segmentation	17
Figure 2.6: Interactive thresholding in ANALYZE™ software	18
Figure 2.7: Canny derivatives	20
Figure 2.8: (a) Original MR coronal slice (b) results of segmenting the gray mater	21
Figure 2.9: Multispectral segmentation: (a) Supervised (b) Unsupervised	23
Figure 2.10: Intra-operator variability for 3 supervised methods	25
Figure 2.11: Examples of the results for different multi-spectral methods with corresponding raw MR image data	28
Figure 2.12: A 3D reconstruction of tumor, ventricles and head	29
Figure 2.13 : Supervised and unsupervised image segmentation schemes	30
Figure 2.14: An example of Halcon package	32
Figure 2.15: A schematic of a CT setup	35
Figure 2.16: Evolution of the X-ray CT systems	36
Figure 2.17: Magnetic nuclei behave like microscopic bar magnets	38
Figure 2.18: Vector representation of magnetization in the presence of an applied field	39
Figure 2.19: Transformation between spatial and frequency domain	39
Figure 2.20: Magnetization vector after undergoing the RF pulse application process. ..	41
Figure 2.21: MR imaging technique	42
Figure 3.1: The instrument used by Swanson to obtain brain slices	44
Figure 3.2: Reference points of Swanson Atlas	45
Figure 3.3: Complexity of the rat brain and slice density	46
Figure 3.4: Original Nissl-stained brain and Freehand drawing of it	47
Figure 3.5: Preview mode in AI®	50
Figure 3.6: An example of un-connected spline in the brain map	51
Figure 3.7: Overlapping regions in rat brain atlas	51
Figure 3.8: Extra symbols of the rat brain atlas	52
Figure 4.1: A sample of part of CDL data format	55
Figure 4.2: Spline Approximation 1	59
Figure 4.3: Spline Approximation 2	60
Figure 4.4: Node merge	61
Figure 4.5: Merging redundant elements	63
Figure 4.6: Line crossing algorithm to identify regions defined by line segments	66
Figure 4.7: Using seed points for identification of tissues	67
Figure 4.8: Finding the isolated islands	67
Figure 4.9: Removing the void loops	68
Figure 4.10: Level 26 of the rat brain after segmentation	70

Figure 4.11: AI^{TM} drawing of level 26.	70
Figure 4.12: Superposition of the results on the original drawing file.	71
Figure 14: Volume Segmentation	73
Figure 4.15: Flowchart of integration of the results	74

1. Introduction

1.1 Medical Imaging

Medical imaging is a rapidly evolving field, especially in those aspects influenced by advances in digital computer technology. This evolution makes hospitals, clinics, and health care centers adopt new imaging instrumentations in ultrasound, X-ray tomography and nuclear medicine which in turn requires a great deal of knowledge and skills in handling the medical image data [1].

The study of medical imaging is concerned with the interaction of all forms of radiation with tissue and the development of appropriate technology to extract clinically useful information from observation of this interaction. Such information is usually displayed in an image format. Medical images can be as simple as a projection or shadow image – as first produced by Röntgen more than 100 years ago – or as computer reconstructed image – as produced by computerized tomography (CT) using X-ray or by magnetic resonance imaging (MRI) using intense magnetic fields. Although, strictly speaking, medical imaging began in 1895 with Röntgen's discoveries of X-rays and the ability of X-rays to visualize bones and other structures within the living body [2], contemporary medical imaging began in the 1970s with the advent of computerized tomography [3][4].

Early medical imaging utilizes images that are a direct manifestation of the interaction of some form of radiation with tissue. For example, conventional X-ray

procedures transmit a beam of radiation through the patient onto a film. The developed film provides a shadow image of the patient which is a direct representation of the tissue specific absorption and scatter of the X-ray beam through the body.

Nowadays, by means of powerful computational techniques and facilities, other types of interaction with tissues are explored and new methods of imaging are developed, such as: Computer Tomography (CT), Positron Emission Tomography (PET) and Magnetic Resonance Imaging (MRI).

1.2 Segmentation

1.2.1 Introduction

One of the primary applications of the medical imaging is pathology. The information obtained by different methods of imaging (i.e. MRI, CT, PET) can be extensively used to visualize the tissue in question and it helps physicians obtain information about the disease, such as tumor volume. However most of these methods provide 2-dimensional images. Consequently, 3-dimensional reconstruction strategies are required Figure 1.1. This job demands knowledge of different physiological regions in the image and delineating them. The data extraction from medical images and its conversion to useful information such that it can be used for diagnosis of the disease requires classification and labeling of the data, which is called segmentation.

Segmentation is also used in other fields such as Machine Vision, Astronomy, and Satellite Imaging [38]

1.2.2 Segmentation

Subdividing an image into meaningful regions and labeling those regions for use in further analysis of the image is called segmentation. It is hoped that the regions obtained correspond to the physical parts or objects of a scene represented by the input image.

There are different methods for segmentation of an image. Segmentation can be done by comparing the image with a standard set of images or superimposing the image onto a standard and then extracting the segmented boundaries. It can also be done manually by an operator who has enough expertise in the area to understand the image as well as distinguish different regions in it. Also knowledge-based methods can be used to facilitate the computerized image segmentation. Figure 1.2 shows an example of color image segmentation. As it can be seen, the results of computer segmentation do not always comply with what the human brain can achieve.

Segmentation has gained critical importance in the following medical applications:

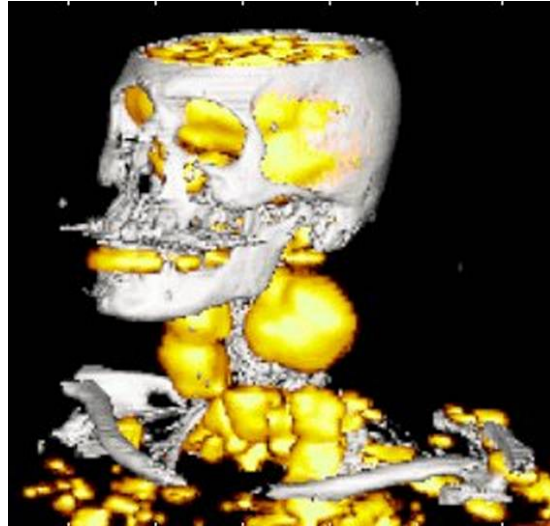


Figure 1.1: 3D reconstruction of human skull using CT images [50]

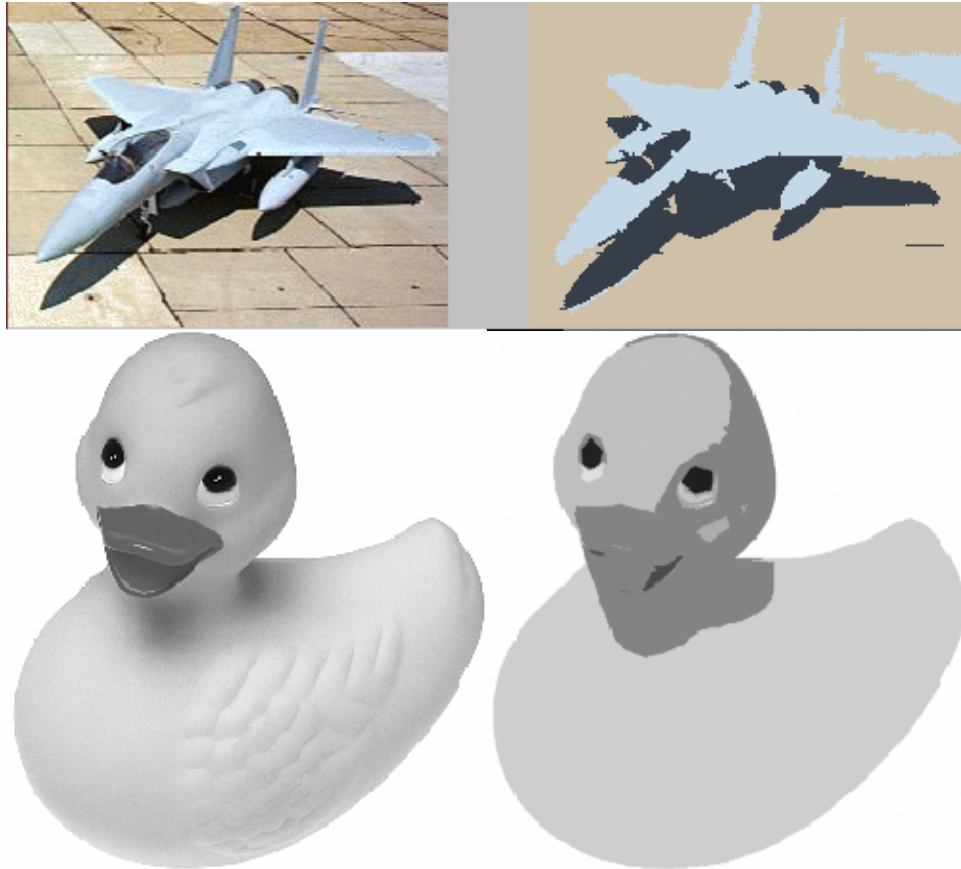


Figure 1.2: Two examples of segmentation [49]

1. Identifying anatomical areas of interest for diagnosis, treatment and surgery planning:
2. Measurements of tumor volume and its response to therapy
3. Virtual surgery for training purposes before operation as well as robotic surgery.
4. Preprocessing for multimodality image registration, such as identifying the locations of important functional regions of the brain as required for applications such as optimal surgical planning by images obtained from functional MRI or Electro-encephalogram (EEG).
5. Improving the correlation of anatomical areas of interest with localized functional metrics

Segmentation is a critical component within an image analysis system, Figure 1.3. It assists us in better understanding and interpretation of the data in the image.

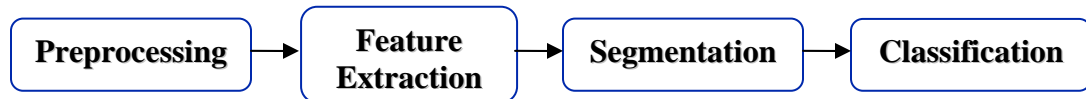


Figure 1.3: Flowchart of an image analysis system

More detailed information on different type of preprocessing, feature extraction and segmentation is provided in chapter 2.

1.3 Purpose of Research

Magnetic Resonance Imaging (MRI) is an imaging method used by physicians and radiologists to view internal body structures using synchronization of radiowaves and magnetic fields. An MR magnet unit is a large noninvasive device which utilizes the properties of magnetism to create nondestructive, images of internal soft tissues of the body, including the brain, spinal cord and muscles. MRI gives physicians and researchers a very powerful tool to see and study the health state of internal organs of body; even it enables them to trace their activities. In order to take the most advantage of MR images, one needs to extract feature information about the tissues and organs which have been imaged.

Atlases of human/animal body have been used to accomplish the task of delineating MR images. A segmented atlas can be extremely useful in clinical applications as well as research. Segmentation is a major part of an image analysis process and will be discussed in depth in chapter 2.2 of this thesis.

For example, in radiotherapy the volume measurements and the localization of several individual brain structures is a necessary step. An atlas based segmentation of the MR image set of the patient's brain is appealing to physicians because they are able to segment several structures simultaneously, while preserving the anatomical topology [44][45]. Without the use of segmented atlases and numerical algorithms, estimation of the tumor volume from MR image set is an extremely difficult task. Frequently, image

datasets can be registered or aligned against segmented atlases to further assist medical analysis. These atlases can be prepared both in 2 dimensions and 3 dimensions and once the alignment has been done, various regions or volumes of interest can be delineated. A segmented atlas is widely being used as reference for functional MRI, in which scientists study the activity of the brain and its reactions to different stimuli.

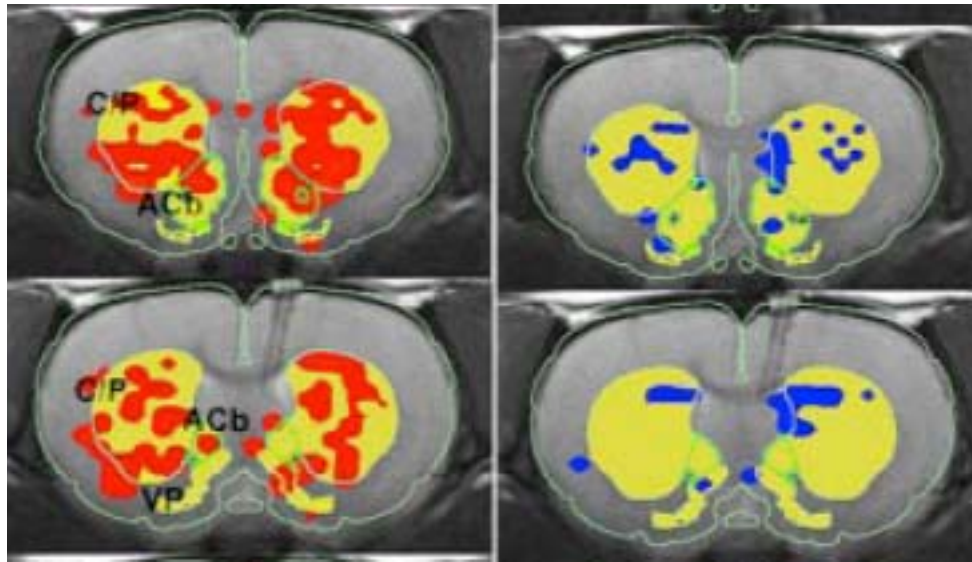


Figure 1.4: Application of a Segmented Atlas in an fMRI Study. The images show positive and negative brain activity within the brain in response to pup stimulation in a lactating dam [46].

In addition to a visual comparison of image and atlas by an expert, various attempts have been made to delineate tissues in an image against a reference atlas via computers. Most frequently, authors use individual slices of an atlas to perform manual segmentation. Although the resulting segmented regions can show atlas tissue structures which are visually informative but they can be neither considered numerically consistent nor used in a 3D extrapolation algorithm to generate a fully segmented 3D digital brain.

In this work, we process each slice of the atlas automatically and extract all the numerical information provided within the atlas to create numerically robust 2D delineations suitable for further processing and analysis.

The atlas used in this work was prepared in *Adobe Illustrator*, which stores the information based on their mathematical description and vector information rather than pixel based information [40]. Numerous algorithms were developed and applied to each slice of atlas to create numerically consistent 2D brain maps. Many of these routines addressed flaws and discrepancies within the atlas data structure.

Spline curves, lines and text labels were major geometric entities used to delineate tissue boundaries within each atlas slice. However, several flaws needed to be resolved before the segmentation process could take place:

1. Multiple lines and curves bundled into a single boundary
2. Non-intersecting or over-extended spline segments
3. Overlapping regions
4. Functional or physical areas labeled remotely from the region
5. Regions without any anatomical label

Each slice of the atlas would be processed to address the above issues. Then using the text label positions as seed points, the segmentation process would determine tissue types of each brain slice. More than 1200 regions were identified and labeled for the rat brain atlas. Finally we will store the information of the segmented atlas slices in

individual files containing coordinate information as well as tissue type of the brain so they can be used in a 3D reconstruction algorithm. More detailed information is provided in chapter 4.

In following section, a brief review of various segmentation strategies is provided.

2. Background

2.1 Introduction

Recent advances in medical imaging systems have resulted in significant improvements in the areas of anatomical, functional, and dynamic imaging procedures. The generation of new methods provides an increasing array of multi-spectral data sets that contain unique features important for tissue segmentation and classification [1][2]. Similarly, multimodality imaging methods (MRI, X-ray, CT and PET) provide a means for correlation of anatomical and various functional metrics associated with each imaging modality. In this context, image segmentation becomes an important step in the process of image analysis.

2.2 Segmentation: Methods and Applications

As previously shown in Figure 1.3, image segmentation is part of an image analysis system. A successful segmentation consists of the following two steps:

1. Preprocessing
2. Feature Extraction

Preprocessing improves the quality of the data by reducing artifacts. Feature extraction and selection provides the measurement vectors on which the image segmentation is based. Segmentation groups pixels into regions and hence defines the

boundaries of the tissue regions. Finally segmentation is followed by classification or labeling of the regions into the tissue types.

2.2.1 Preprocessing

As in all scientific and engineering areas, nothing can be done perfectly. In imaging, independent of the selected method, there are always imperfections and flaws in the final image due to the inherent technical limitations of the imaging process which can substantially affect the following results of image analysis.

For example, in magnetic resonance imaging, the following major problems need to be addressed prior to segmentation [6]. To illuminate these problems a circular phantom of water was used as the object to be imaged using altered parameter settings to cause specific distortion in the image.

The major distortions resident in an MR image are:

1. Random image noise
2. RF field non-uniformities (Figure 2.1)
3. Susceptibility

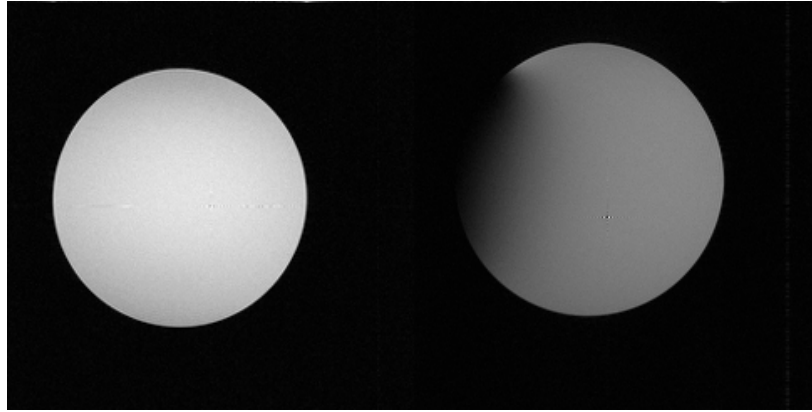


Figure 2.1: RF field inhomogeneity effect [6]

The first two sources of error are self explanatory. Susceptibility occurs when a metallic object is close to the magnetic field. The metallic object is too small, or too poorly conductive, to cause significant RF inhomogeneity, but it does distort image in a different way.

In CT images, similar problems exist. For example, if the transmitted beam has a low radiation dose and the number of data collected for one slice is not sufficient, then a noisy result will be obtained, Figure 2.2. Another problem in CT images can be the presence of a metallic object in the body such as dental fillings. These objects have attenuation values which exceed that of CT systems can faithfully image resulting in a streaking effect. The appearance may mimic a “splashing” effect from the middle of the structure towards the edges of the object scanned, Figure 2.3,

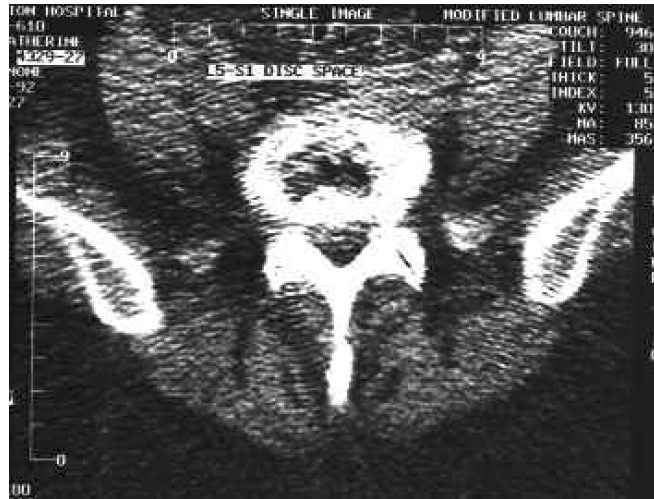


Figure 2.2: A noisy CT image due to low dose beam [7]



Figure 2.3: Streaking artifact due to external metal objects, in this case dental filling [7]

More comprehensive and complete coverage of the contributing sources of errors can be found in Plante's work [8].

When implementing a particular image processing technique, there are some fundamental considerations to address. These include the amount of information loss, the

signal to noise ratio, edge and fine detail degradation and to a lesser extent computational complexity and time.

2.2.2 Feature extraction

Segmentation of images is based on sets of features that can be extracted from the images, such as pixel intensities which in turn can be used to calculate other features such as edges, and texture. Rather than using all the information in the images at once, feature extraction and selection breaks down the problem of segmentation to the grouping of feature vectors [9], thus selection of good feature is the key to successful segmentation.

There are 2 major features which make the foundation for the rest [5]:

1. Pixel intensity-based features:
2. Edge and texture based features:

In first method, the gray scale value of the pixel is used as the feature. The pixel intensity input can come from a single image, a volume data set or a multi-spectral data set of the same anatomical location (multi-spectral images are usually obtained by a multiple sequences of imaging).

Due to non-uniform nature of medical images, a global threshold cannot segment the data and additional features are required. Some researchers have used edge detection methods [10],[11]. In this method a convolution of the image with 2nd derivative of a Gaussian function is deployed:

$$C(x, y) = \nabla^2 (I(x, y) \times G(x, y, \sigma)) \quad (2-1)$$

where

$I(x, y)$ is an image,

$G(x, y, \sigma) = \frac{1}{2\pi\sigma^2} e^{-\frac{(x^2+y^2)}{2\sigma^2}}$ is a Gaussian function

$C(x, y)$ is the counter image

This is the base for edge detection method on which improved edge detection methods can be built. Canny edge detection method [12] is one of the popular improved ones but there have been disputes about reliability of edge detection segmentation [5].

Figure 2.4 shows an example of Canny's method.

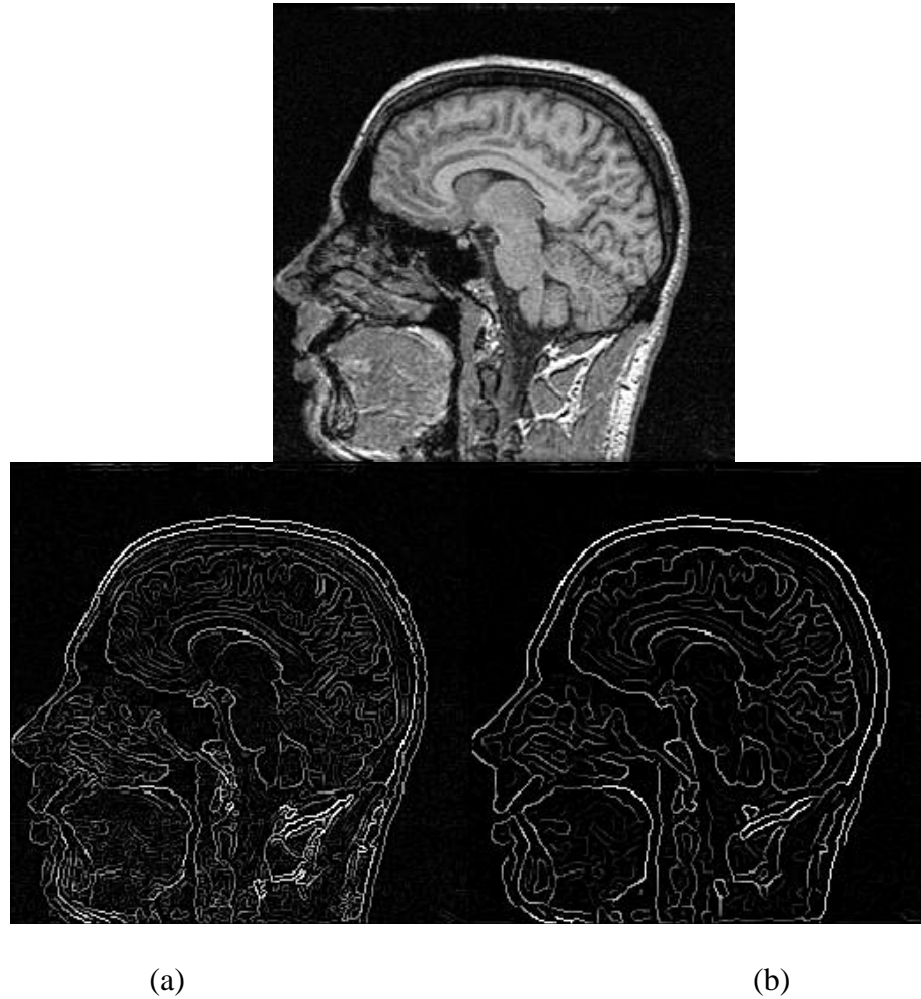


Figure 2.4: Edge Detection using Canny operator, top is the original image (a) $\sigma = 1$ (b) $\sigma = 2$ [12]

Another feature reported in the literature is texture [14][15]. Texture is a statistical feature necessarily derived from a large number of pixels; hence it is not suited for pixel classification. The main application of texture feature detection is in classification area rather than delineation of regions.

2.2.3 Segmentation

The image segmentation can be roughly divided into two categories: a single image, or gray scale, segmentation where a single 2D or 3D image is used and multi-spectral image segmentation where multiple images with different gray scale contrast are available. Figure 2.5 gives a general overview of these categorizations.

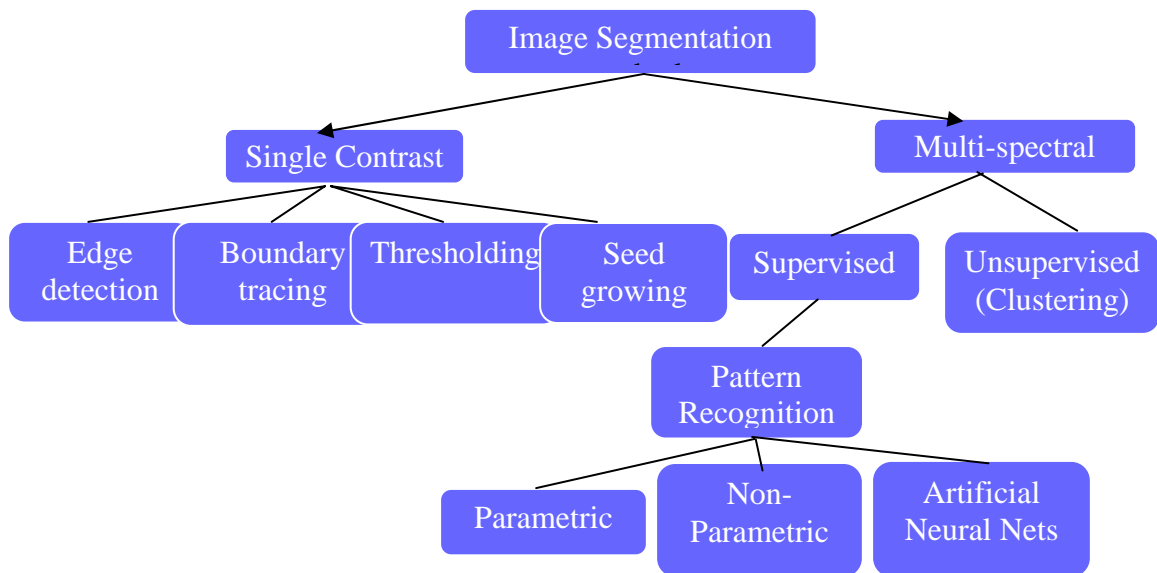


Figure 2.5: General classification of segmentation [5].

In the following sections, each method is explained with the emphasis on the application of the method on MR images.

2.2.3.1 Single contrast segmentation

Gray scale segmentation methods may provide some useful information but they are generally limited to relatively simple structures.

2.2.3.1.1 Threshold-based methods

The most intuitive approach to segmentation is global thresholding, which has also been performed on X-ray and CT data. One common difficulty with this approach is determining the value of the thresholds. One resolution for this issue is interactive selection of the threshold in which the operator specifies the value of threshold and sees the results of the process on the fly so he/she can decide on the desired value. A popular implementation of this method can be found in ANALYZE software [16].

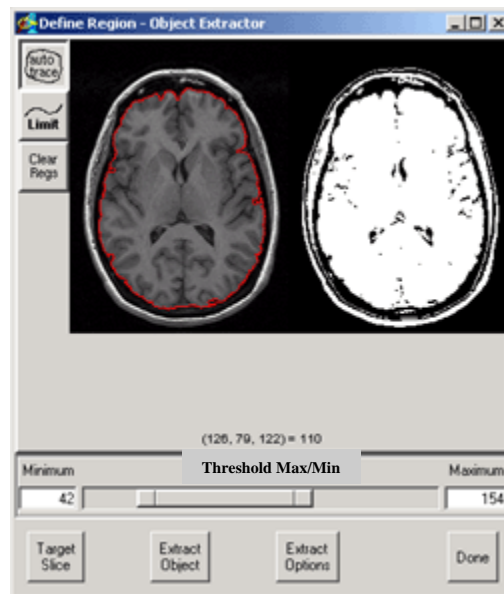


Figure 2.6: Interactive thresholding in ANALYZE™ software [16]

This method is limited by the variability of anatomy and MR data as well as image artifacts (see section 2.2.1). Hence some researches have tried to combine thresholding with knowledge-guided methods where global thresholds are determined based on a “goodness function” describing the separation of background and the

tissue/organs, such as skull or brain [17]. Since this method is not a very robust method, it has stimulated interests in the application of other approaches.

2.2.3.1.2 Edge based methods

In this method a pixel is selected in a region to be outlined, and then the method finds a point on the boundary of the region and follows the boundary from that point. Several ways are open to the operator to optimize the result for non-ideal cases.

The disadvantage of this method is the sensitivity to noise in the image. It also suffers from incorrect detection of edges due to over and under-segmentation, and variability in threshold selection in the edge image. Boundary tracing schemes in general are to be restricted to segmentation of large, well defined structures such as the brain parenchyma, but not to distinguish individual tissue types. The following figures depict the implantation of Marr-Hildreth operator on a brain MRI [14][18]

As mentioned previously, Canny edges are estimated by convolution of the image with the Gaussian operator. In one dimension, the Gaussian function, its first derivative and its second derivative, are given in Eq. (2-2):

$$\begin{cases} G(x) = \frac{1}{\sqrt{2\pi}\sigma} \exp\left(-\frac{x^2}{2\sigma^2}\right) \\ G'(x) = \frac{1}{\sqrt{2\pi}\sigma^3} \exp\left(-\frac{x^2}{2\sigma^2}\right) \\ G''(x) = \frac{1}{\sqrt{2\pi}\sigma^3} \exp\left(-\frac{x^2}{2\sigma^2}\right) \left(1 - \frac{x^2}{\sigma^2}\right) \end{cases} \quad (2-2)$$

The equivalent 2-D functions are expressed most easily with respect to the polar coordinate system, where the radius r is $\sqrt{x^2 + y^2}$ (see Eq. (2-3)). The function is symmetrical. The three polar equations, Gaussian function, first derivative and second derivative are given in Eq. (2-3). Figure 2.7 shows the Canny derivatives.

Figure 2.8 shows the results of running the Canny edge operator to estimate the boundaries of gray mater in the coronal slice of the human brain that has a tumor. Canny's operator is too sensitive to noise and thus it is likely to estimate the false edges.

$$\begin{cases} G(x) = \frac{1}{\sqrt{2\pi}\sigma} \exp\left(-\frac{r^2}{2\sigma^2}\right) \\ G'(x) = \frac{1}{\sqrt{2\pi}\sigma^3} \exp\left(-\frac{r^2}{2\sigma^2}\right) \\ G''(x) = \frac{1}{\sqrt{2\pi}\sigma^3} \exp\left(-\frac{r^2}{2\sigma^2}\right) \left(1 - \frac{r^2}{\sigma^2}\right) \end{cases} \quad (2-3)$$

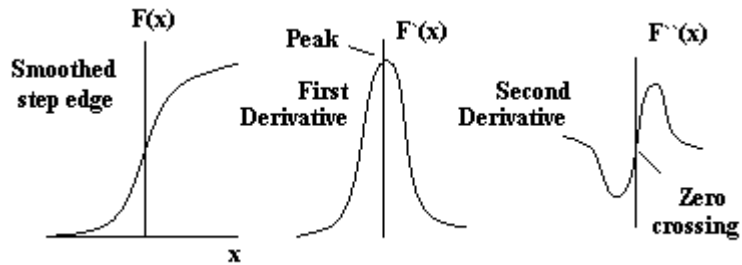


Figure 2.7: Canny derivatives. Left: original signal. Middle: first derivative. Right: second derivative ($F(x)$ is the convolution function)

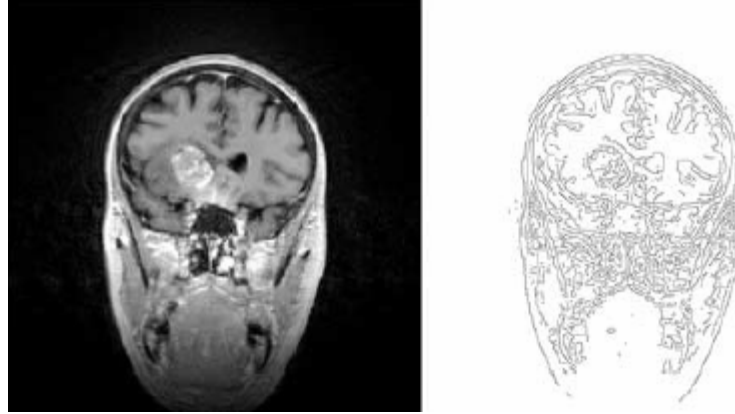


Figure 2.8: (a) Original MR coronal slice (b) results of segmenting the gray matter boundary in a 2D coronal slice using the Canny operator [12]

2.2.3.1.3 Seed growing methods

This method requires an operator to empirically select seeds and thresholds. Pixels around the seeds are examined and included in the region if they are within the thresholds, sometimes adding the requirement that they are sufficiently similar to the pixels already in the region. Each added pixel then becomes a new seed whose neighbors are inspected for inclusion in the region. Also, there are some reports that this method is used to operate on segmented data as a post processing step to reduce “noise” in the segmentation and improve the appearance of the 3D reconstruction.

As with all single image methods, in practice only well defined regions can be robustly identified. The method is commercially available in ANALYZE™ package.

2.2.3.2 Multi-spectral segmentation

The most common approach for Multispectral segmentation is pattern recognition [19][24]. These techniques generally appear to be successful particularly for brain images, but much work remains in the area of validation. These methods can be applied for normal tissues as well as neuro-psychiatric disorders where the MR parameter distributions have the same characteristics as those for normal tissues. More difficult problems can be encountered with the segmentation of complex pathology such as glioblastoma.

The difference between supervised and unsupervised methods is important due to the need for reproducible measurements. Supervised methods require operator input for segmentation. This can be done by selecting training pixels or training regions on the images. Unsupervised methods are automatic, in the sense that operator intervention may be necessary to complete the process but the result should be operator independent.

Figure 2.9 shows the difference between the two approaches. In part (a) – supervised – of the figure the input data consists of the features selected in the preceding step. An unsupervised method defines regions in the image without operator input. However these regions do not have anatomical meaning associated with them, thus a classification step is necessary to come to a labeled output image.

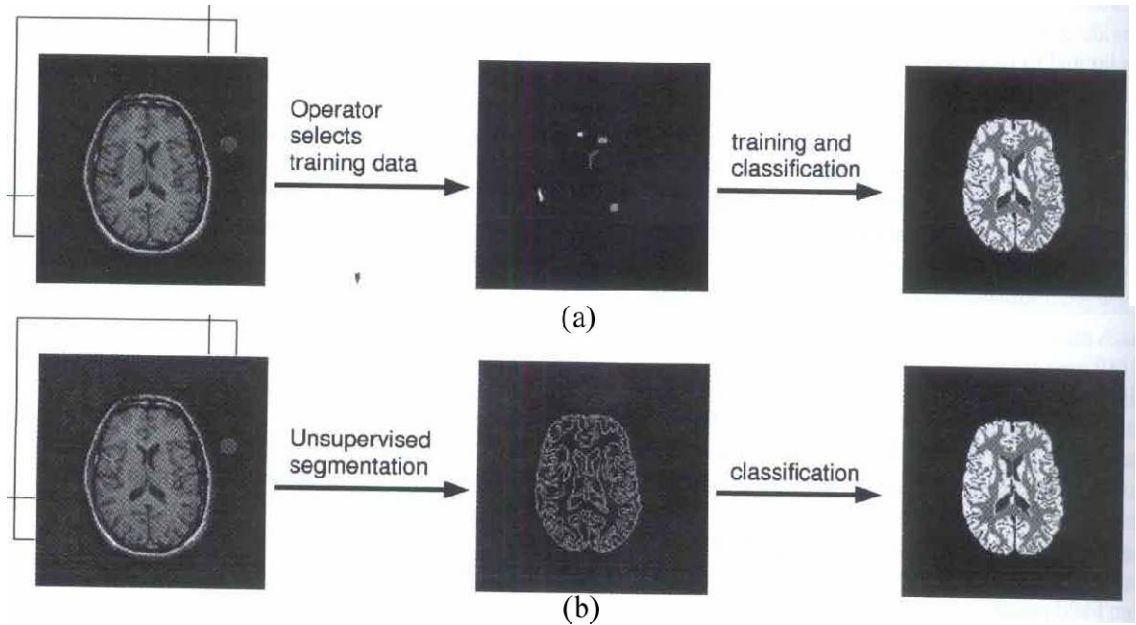


Figure 2.9: Multispectral segmentation: (a) Supervised (b) Unsupervised [5]

2.2.3.2.1 Pattern recognition methods

Supervised methods include several pattern recognition techniques. Many pattern recognition methods are assuming particular distribution of the features and are called parametric methods. For example, the maximum likelihood method commonly assumes multivariate Gaussian distributions [20][21][22]. This classifier is based on Bayes decision rule which maximizes the a posteriori probabilities. It is the procedure of finding the value of one or more parameters for a given statistic which makes the known likelihood distribution a maximum.

Nonparametric methods, such as k nearest neighbors (kNN) do not rely on predefined distributions, but on the actual distribution of the training samples. Given a training data set consisting of N prototype pattern (vectors) of dimension D and the

corresponding correct classification of each prototype into one of C classes, a pattern x of an unknown class is classified as class c if most of the k closest prototype patterns are from class c [25][26]. Distance is measured with a distance metric appropriate to the problem domain. This method is effective for the multi-channel image data commonly used in medical imaging and remote sensing applications. This method has higher accuracy and stability for MRI data than other common statistical classifiers but the CPU load is higher [26].

Another method in nonparametric approach is Artificial Neural Network (ANN). An ANN is a massively parallel architecture made up of a number of units, which are linked by some connections. These units are capable of accepting incoming signals, performing some Boolean or arithmetic processing on the data and sending signals out over some or all of the connections. The storage of “knowledge” is accomplished by altering the weight associated with each connection.

2.2.3.2.2 Algebraic Methods

Outside the field of pattern recognition, algebraic methods have been reported. For images with clearly identified signature vectors these methods provide an elegant solution to deal with the partial volume effect, which may have some influence on volume measurements. Algebraic methods, however, may become impractical for images showing complex pathology.

All supervised methods are operator dependent. Inter- and intra- operator variability has been measured and shown to be relatively large [20]. An example of this variability is shown in Figure 2.10. An operator selected training data for the same MR image data set on 5 different occasions. The resulting 5 segmentation are compared in the graph in terms of the variability in the classification of individual pixels, evaluated for each tissue class. Shown is the percentage of pixels that are assigned to a particular class compared with the number of pixels that is assigned to that class at least once.

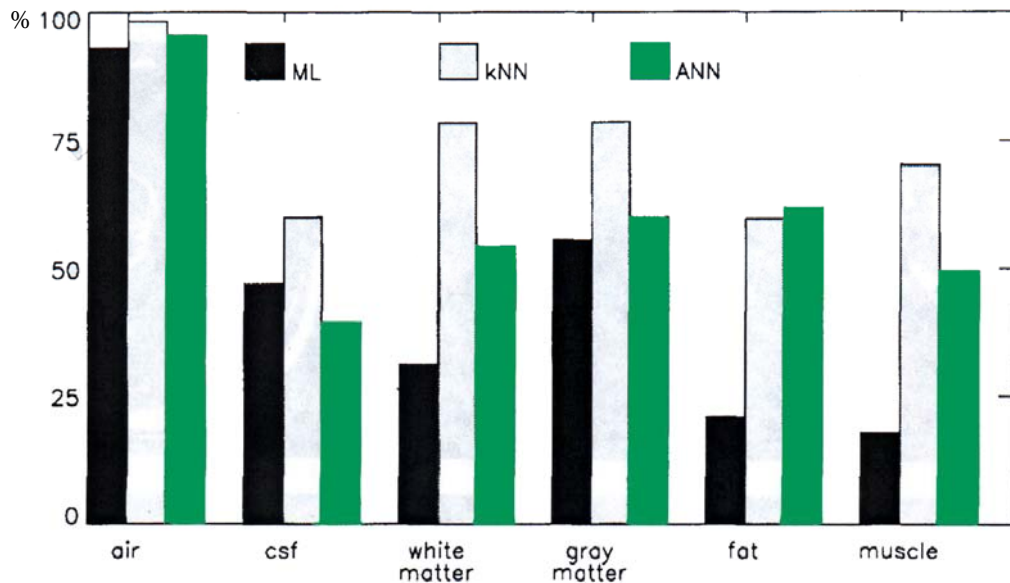


Figure 2.10: Percentage of intra-operator variability for the 3 supervised kNN, ML and ANN methods [5]

2.2.3.2.3 Unsupervised segmentation

Unsupervised methods, also called clustering, automatically find the structure in the data. A cluster is an area in feature space with high density. Mathematically, this can

develop in different ways [27]. Among the different methods in this area, the major ones are k-means and its fuzzy equivalent, fuzzy c-means (FCM). In k-means clustering algorithm the value of k should be decided in advance.

Unsupervised methods show promise for tumor volume determination, but initialization is important for meaningful clustering results and reduction of computation times. This method shows superior results to kNN method.

A brief explanation of fuzzy c-means method applied in clustering is presented, but for more information see [29].

Let R be the set of real numbers, R^p the set of p tuples of real numbers, R^+ the set of non-negative reals, and W_{cn} the set of real $c \times n$ matrices. R^p will be called feature space, and elements $x \in R^p$ feature vectors; feature vector $x = (x_1, x_2, \dots, x_p)$ is composed of p real numbers. Now let X be a subset of R^p . Every function $u : X \rightarrow [0,1]$ is said to assign each $x \in X$ its grade of membership in the *fuzzy set* u . The function u is called a fuzzy subset of X [30].

Note that there are infinitely many fuzzy sets associated with the set X . It is desired to “partition” X by means of fuzzy sets. This is accomplished by defining several fuzzy sets on X such that for each $x \in X$, the sum of the fuzzy memberships of x in the fuzzy subset is one. This can be mathematically expressed as following definition.

Given a finite set $X \subseteq R^p$, $X = \{x_1, x_2, \dots, x_n\}$ and an integer c , $2 \leq c \leq n$, a fuzzy c partition of X can be represented by a matrix $U \in W_{cn}$ whose entries satisfy the following conditions.

1. Row i of U , say $U_i = (u_{i1}, u_{i2}, \dots, u_{in})$ exhibits the i^{th} membership function (or the i^{th} fuzzy subset) of X
2. Column j of U , say $U^j = (u_{1j}, u_{2j}, \dots, u_{cj})$ exhibits the values of the c membership functions of the j^{th} datum in X
3. u_{ik} shall be interpreted as $u_i(x_k)$, the value of the membership function of the i^{th} fuzzy subset for the k^{th} datum.
4. The sum of the membership values for each x_k is one (column sum $\sum_i u_{ik} = 1 \forall k$)
5. No fuzzy subset is empty
6. No fuzzy subset is all of X

The fuzzy method, as well as k-means method, is capable of yielding highly reproducible results.

Figure 2.11 shows results for segmentation methods described. Three images, the Multispectral MRI data set, of one slice of a patient with glioblastoma treated with radiation and chemotherapy are shown in Figure 2.11a-c. It can be seen in Figure 2.11d-i that unsupervised methods do not always converge to anatomical tissues. For example, in Figure 2.11g, FCM method did not separate cerebrospinal fluid (CSF) and edema. 2

methods, partial supervision and validity-guided re-clustering, are proposed in Figure 2.11h and Figure 2.11i, respectively. Figure 2.11e shows a kNN result in which the white matter has been underestimated, most likely a result of the high operator dependency of this method. A 3D reconstruction of this dataset after k-means segmentation is shown in Figure 2.12.

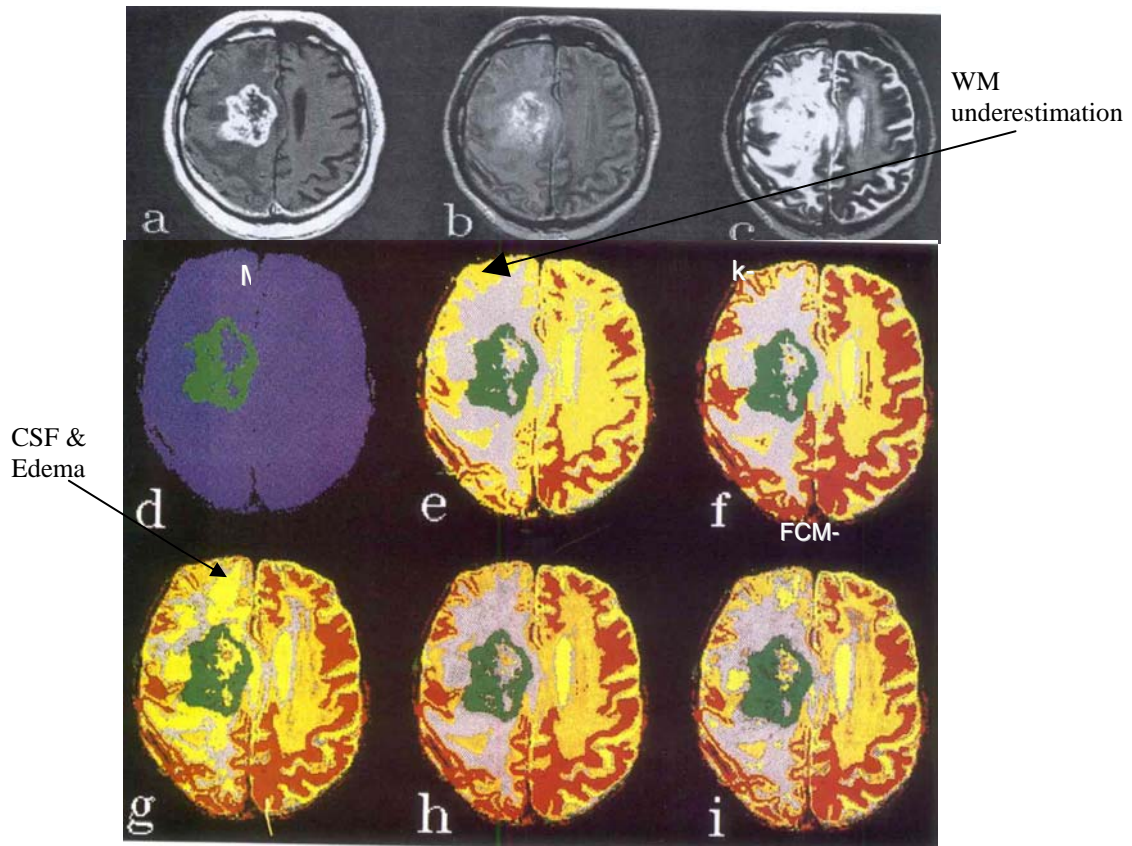


Figure 2.11: Examples of the results for different multi-spectral methods with corresponding raw MR image data [5]

There have been efforts in the field for improving the results of the unsupervised segmentation. The most noticeable one is the employment of a priori knowledge about the image. The methods can be optimized by insertion of implicitly heuristics or by use of

an explicit knowledge base. The knowledge used in the medical image (specifically MRI) segmentation is acquired mainly by using training data rather than through interaction of a knowledge engineer with an expert, i.e., a radiologist. To name a few of the features that can be used in MRI segmentation is the image gray level, size, position and shape of the regions as well as anatomical constraints on neighboring regions.

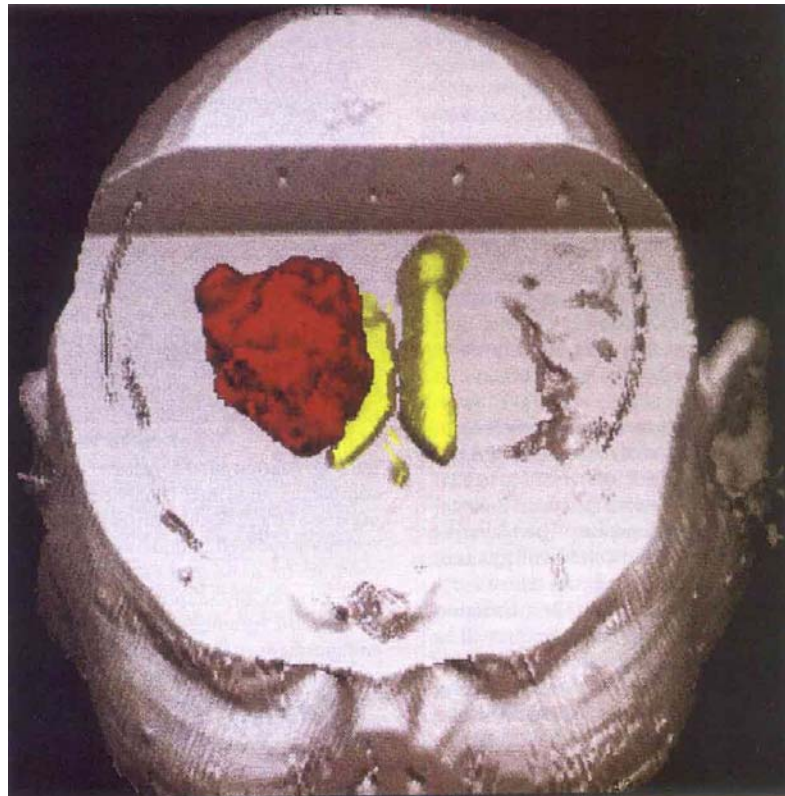


Figure 2.12: A 3D reconstruction of tumor, ventricles and head. The tumor has pushed the right ventricles down [5]

Finally, one can summarize the flow of the segmentation of multi-spectral image as in [5]:

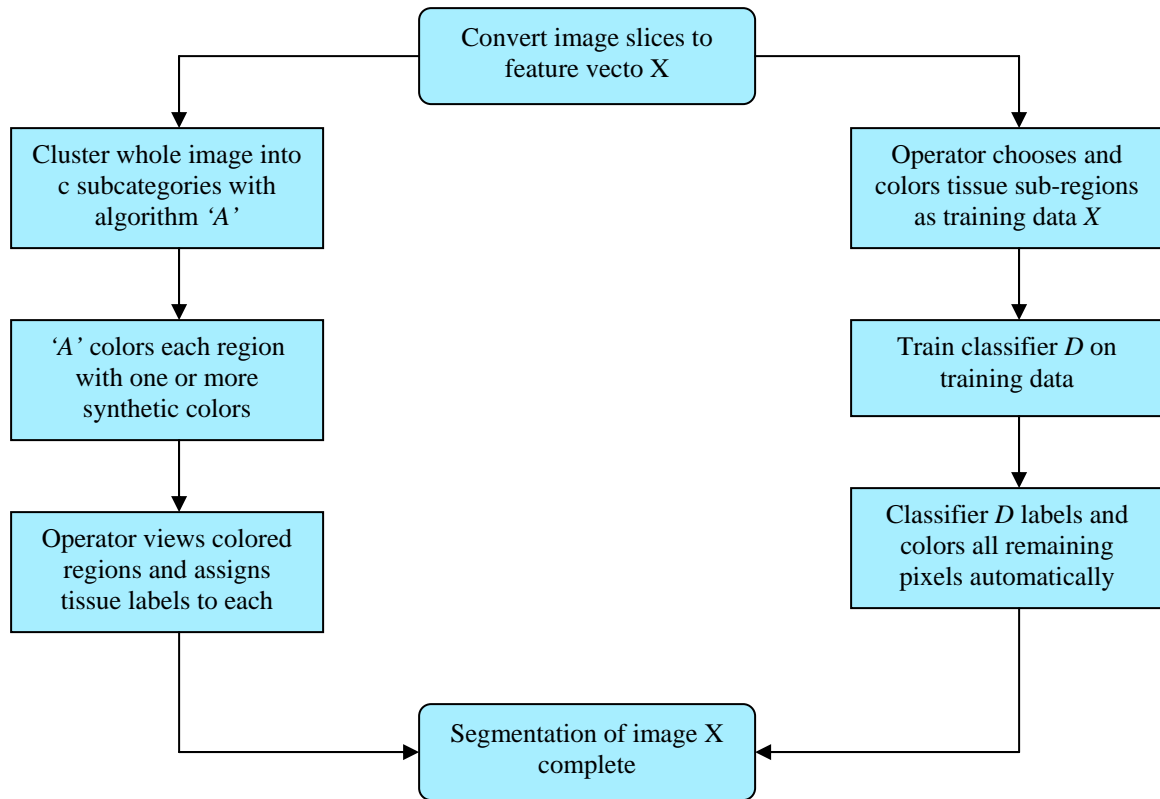


Figure 2.13 : Supervised and unsupervised image segmentation schemes [19].

2.2.4 Classification

Image segmentation refers to the decomposition of an image into regions, but strictly speaking it does not classify the tissue types. Classification is the step that labels the regions. In supervised segmentation, this is done by an operator when labeling training data, where pixels are associated with anatomical tissues. Unsupervised methods return a segmented image with different “classes,” but the association of classes with tissue types must still be performed. Most commonly, this association is done by an operator, or implicitly by an interpreting physician. Some researchers used a region

classification scheme using textural parameters [14]. Its success was limited as some user interaction was necessary to correct classification errors even on normal brains.

2.2.5 Available tools

Many previously mentioned methods are available commercially or as free codes. Some of the more popular products include:

1. MEDx™: MEDx is a UNIX based software package used to visualize and analyze 2D and 3D medical image data. The main features of the program include 2D/3D multi-modality registration, fMRI (functional MRI) analysis, Talairach registration, segmentation, region of interest analysis, and 3D visualization [34].
2. Analyze: is the major suite of medical image processing software developed for and used by the Mayo Foundation over the past decade. Like MEDx, Analyze provides a powerful foundation for selective addition and evaluation of new medical image processing algorithms to the capabilities of the Cluster [35].
3. ITK: is an open-source software toolkit for performing registration and segmentation. ITK is implemented in C++. ITK is cross-platform, using the CMake build environment to manage the compilation process. It should be mentioned that ITK is a set of library tools which should be implemented by user (such as in GUIs, graphical user interface) in order to obtain a fully functional medical imaging software package [36].

4. IDL: offers an expansive array of features that make it a data visualization and analysis solution. This tool has few inbuilt functions that can be used for semi-automated segmentation [37].
5. MVTech Halcon: a machine vision tool which has some medical modules. One of the features of this package is that user can add his own functionalities by using either C++ or XML to the program. It has a wide variety of applications from bar code reading to optical character recognition (OCR) (Figure 2.14) to pattern matching [38].

Figure 2.14: An example of image segmentation which has been used in Halcon package to read the bar code data off the label [38]

2.3 Medical Imaging Techniques

2.3.1 Introduction

There are different physics involved in medical imaging and each results in different techniques of human body imaging. Following is a general overview of various methods that can be used to obtain an image of human organs.

1. Imaging with ionizing radiation
 - a) X-ray computerized tomography (CT)
 - b) Nuclear tomographic imaging – Single photon emission computed tomography
 - c) Tomographic nuclear medical imaging – Positron emission tomography
2. Magnetic resonance imaging
 - d) Nuclear magnetic resonance imaging
 - e) Chemical shift and spectroscopic imaging
3. Ultrasound imaging
 - f) Ultrasonic imaging

In the following sections, we will address the most popular clinical methods, which include computerized tomography and magnetic resonance imaging.

2.3.2 Computerized Tomography (CT)

X-ray CT is a product of X-ray technology with advanced computer signal processing and is capable of generating a cross-sectional display of the body. It is, in fact, the origin of the entire CT evolution which began in the early 1970s [31]. The basic principle of the X-ray CT involves X-ray generation, detection, digitization, processing, and computer image reconstruction. X-rays passing through a body are attenuated at different rates by different tissues. The attenuated X-rays are then collected by the detectors and converted to digital numbers or data by the analog to digital converters (ADCs). The digital data are then fed into a computing device for image reconstruction.

Generally the pencil-beam-type X-ray is simply scanned along a line at a given direction or view. To achieve several different angles of perspective or projection data, the scanning is repeated at each given angular view by simply rotating both X-ray tube and detectors. Figure 2.15 shows a schematic of a CT setup.

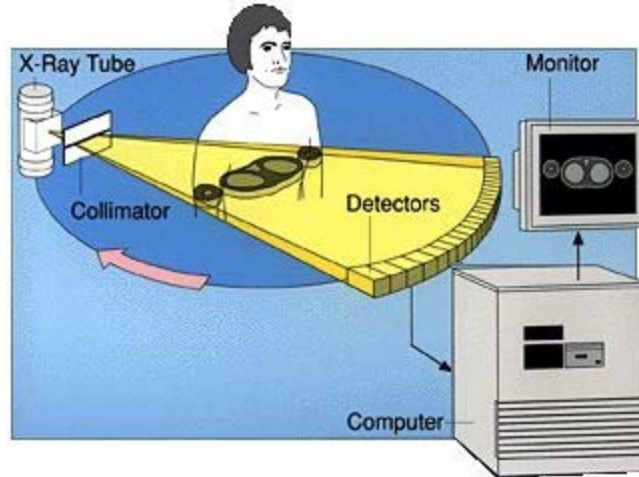


Figure 2.15: A schematic of a CT setup [32]

The photon density that emerges when a narrow beam of mono-energetic photons with energy E_0 and intensity I_0 passes through a homogenous absorber of thickness x can be expressed as [32]:

$$I = I_0 \exp[-\mu(\rho, Z, E_0)x] \quad (2-4)$$

where μ , ρ , and Z are linear attenuation coefficient, density of the absorber, and atomic number, respectively. In the energy region where most commercial X-ray CT systems are being engaged for medical tomography ($\cong 70 \text{ keV}$), two types of interaction are dominant, namely photoelectric absorption and Compton scattering.

In photoelectric interaction the X-ray photon is completely absorbed by transferring all of its energy to an electron. In Compton scattering, on the other hand, scattered X-rays undergo both a directional and energy change.

Since 1972, X-ray CT has evolved from its first generation. Figure 2.16 depicts 4 different configurations of X-ray emitters and detectors.

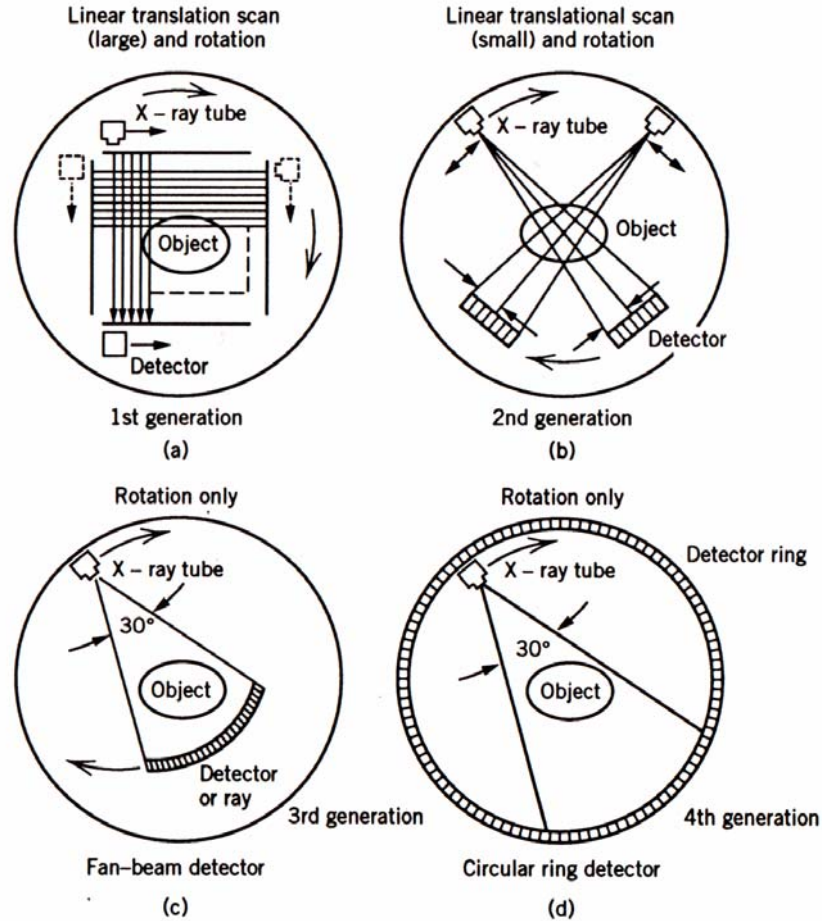


Figure 2.16: Evolution of the X-ray CT systems from the first to fourth generation scanners [32]

2.3.3 Magnetic resonance imaging

Magnetic resonance imaging (MRI) is an imaging technique that is primarily used in medicine to produce high quality images of the inside structure of the human body. It is based on nuclear magnetic resonance (NMR) which is a phenomenon of magnetic

systems that possesses both a magnetic moment and an angular momentum. The NMR is also widely used in chemistry as a spectroscopic technique to characterize the structure of molecules, such as small proteins in solution. The picture produced consists of pixels whose intensity is proportional to the NMR signal intensity of the contents of the voxel of the objects being examined.

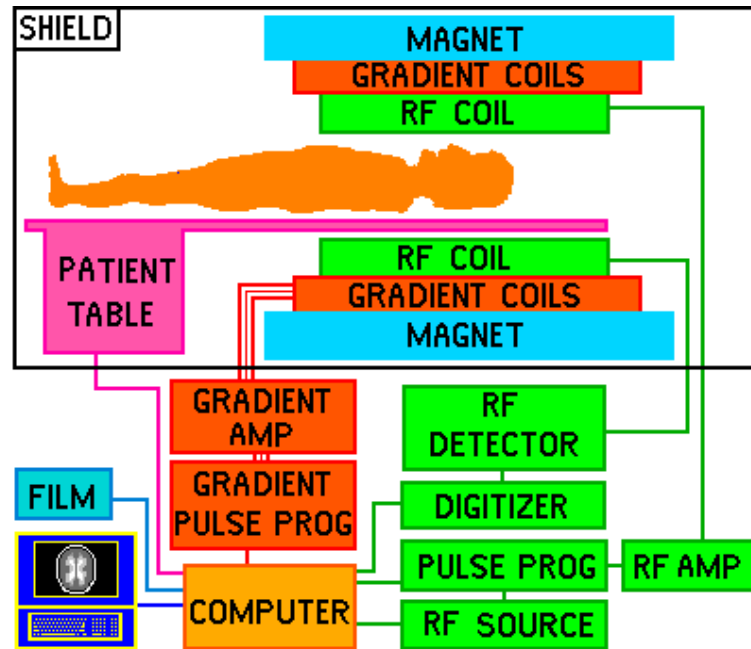


Figure 2.17: Schematic of MR imaging setup [48]

The phenomenon of Nuclear Magnetic Resonance (NMR) was independently discovered by two groups of physicists headed by F. Bloch and E. M. Purcell. The basic physical effect at work in NMR is the interaction between nuclei with a nonzero magnetic moment and an external magnetic field. The nucleus has a magnetic field due to its spin, Figure 2.18, and they have a resonance frequency depending upon the external magnetic

field they are experiencing. This angular frequency can be found via the Larmor's equation:

$$\omega = \gamma \cdot B_0 \quad (2-5)$$

where γ is termed the *gyromagnetic ratio* and is a fundamental property of the nucleus.

Since each atom acts like a tiny magnet bar, they align themselves with the external magnetic field B_0 , Figure 2.19. These tiny magnets can be flipped over upon receiving an RF (Radio Frequency) wave. The angle of tilting can be found by:

$$\theta = \gamma \cdot B_1 \cdot \tau \quad (2-6)$$

where θ is the flip angle, B_1 is the applied RF magnetic field and τ is the time duration of the RF pulse.

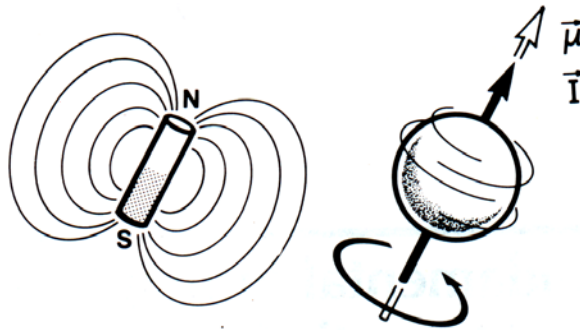


Figure 2.18: Magnetic nuclei behave like microscopic bar magnets [32]

Once the RF pulse is switched off, the nuclei release the absorbed energy at the same frequency as the RF signal. The more number of protons in the tissue, the stronger the released energy gets, which in turn can be detected by the receiving instruments. The

signal, which is in form of electrical current, gets processed by the computer and is interpreted into image.

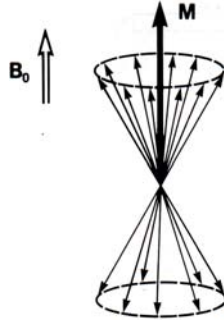


Figure 2.19: Vector representation of magnetization in the presence of an applied field [32]

Since the nucleus is spinning, the observed current is in the form of a free induction decay of a sinusoidal wave. Therefore, in order to transform the frequency domain information of the signal to spatial information of the related tissues, the Fourier transform is necessary, Figure 2.20.

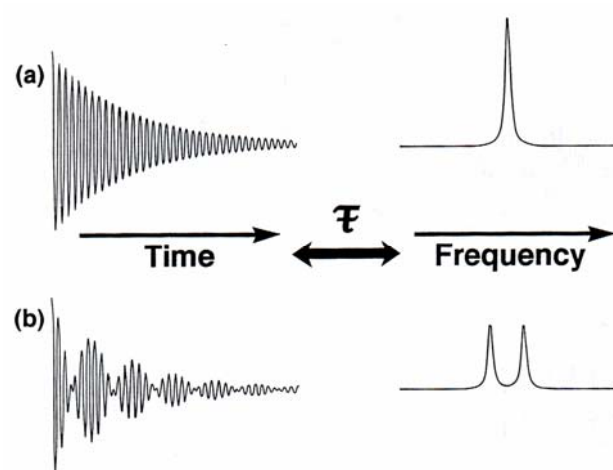


Figure 2.20: Transformation between spatial and frequency domain by Fourier transformation. (a) Time domain to frequency domain of a single signal. (b) The same transformation on a compound frequency signal [32]

Also it can be found that there are two components of the magnetization vector in Figure 2.21 and each of them has their own decay time constant. Therefore one can formulate the strength of the magnetization vector in each direction by the following relations:

$$M_z = M_0 \left[1 - \left(1 - \frac{M'_z}{M_0} \right) \exp\left(\frac{-t}{T_1}\right) \right] \quad (2-7)$$

$$M_{x,y} = M_{x,y}(0) \exp\left(\frac{-t}{T_2}\right) \quad (2-8)$$

where M'_z is the z-component of the magnetization at the initial stage, M_0 is the total magnetization and T_1 , which is termed as relaxation time constant, is the decay constant in z direction. For Eq. (2-8), the relaxation constant is called T_2 and $M_{x,y}(0)$ is the initial component of the magnetization in XY plane.

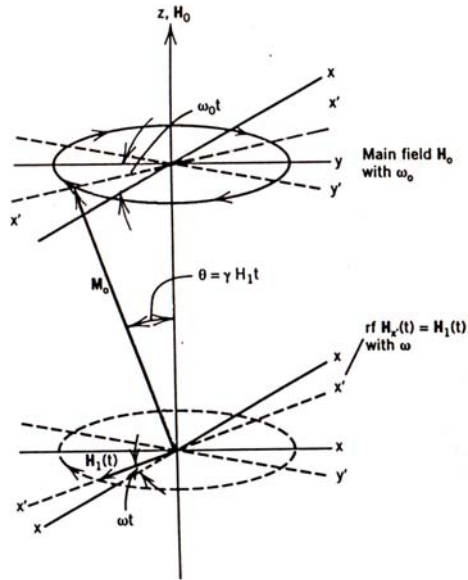


Figure 2.21: Magnetization vector after undergoing the RF pulse application process. Note that in this situation it can be decomposed onto z axis as well as XY plane [32]

The advantages of NMR are, among others,

1. Non-hazardous nature
2. High resolution capability
3. Potential for chemically specified imaging
4. Capability of obtaining anatomic cross-sectional images in any direction
5. High tissue contrast by T1 or T2 (relaxation time differentiation) and
6. Flow related imaging capabilities, such as angiography (Figure 2.22).

Figure 2.17 depicts a schematic setup of the MR imaging system. The patient location can be adjusted by the computer-controlled table to enable imaging different slices throughout the patient body. The magnet shown produces the static magnetic field

B_0 . The heart of the system is the computer which controls all components as well as handles the extensive computations of Fourier transform.



Figure 2.22: MR imaging technique can be used for applications such as angiography [51]

3. Rat Brain Atlas

3.1 Introduction

A common approach to segment an MRI dataset is to use a standard atlas to identify different regions of interests. These atlases are prepared using histological images of brain slices. These drawings can be stored in two different formats; Raster and Vector Graphics. In the raster storage of the data, the image is divided into small units of information, such as color and intensity of image, called pixels. Therefore these types of images have a finite resolution. The other type is raster in which the mathematical information of the image is stored rather than the image itself.

The drawings of the atlases are used to study the basic anatomy of the brain, the fundamental arrangement of the various neuronal cell groups and readily identifiable fiber tracts. Also they are useful as templates of the standardized representation of neuroanatomical data. In other words, they can be used as maps or templates to present in a schematic way, and then compare, results based on the application of various neuroanatomical methods – summaries that can be incorporated into computer graphics databases.

3.2 Swanson Rat Brain Atlas

The core of Swanson's atlas is 73 drawings prepared from transverse Nissl-stained sections through the adult male rat brain. These drawings were created from

photomicrographs of histological sections of a 315 gram adult male Sprague-Dawley rat brain [40]. The animal was deeply anesthetized with chloral hydrate and was perfused transcardially. The brain was embedded in celloidin and sectioned in the frontal (transverse) plane with a sliding microtome, Figure 3.1. The brain was oriented as close to the vertical (longitudinal) plane as possible using the region of the superior sagittal sinus and the base of the brain as guides.

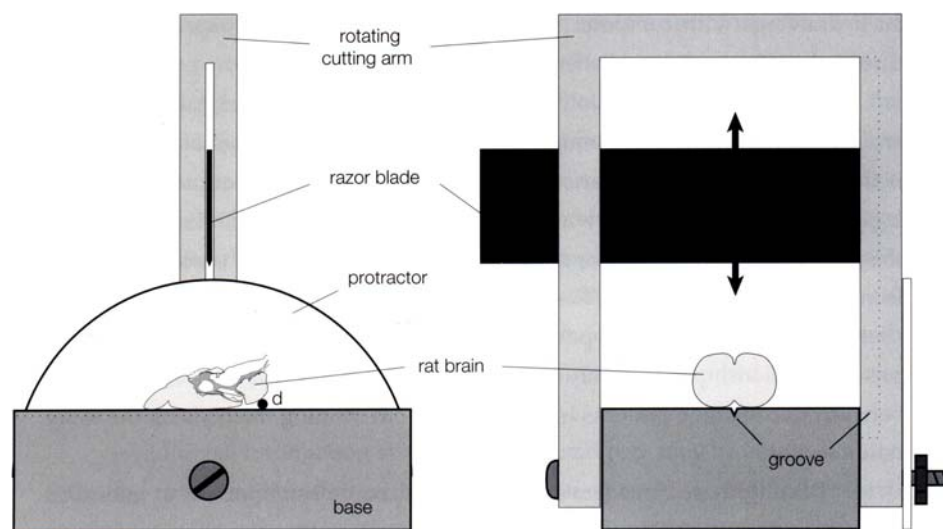


Figure 3.1: The instrument used by Swanson to obtain brain slices [40]

After this step, the slides of photomicrographs were placed in an enlarger with a point light source and an image of sections was projected onto a 4 by 5 inch sheet of film. The global scaling factor is 23:1 for the drawings.

Then using these photos, the original maps were drawn with Adobe Illustrator on a Macintosh computer. For this a copy of the photomicrograph was scanned into a 688 by 510 pixels picture, the original image had a field of view of 11.4mm by 7.8mm. This scanned image was used as a template for tracing the major features of the section. A

microscope was placed next to the computer and all features of the section as well as those on adjacent sections were carefully examined before they were drawn.

It is important to point out that the drawings are not faithful renderings of the section in one major respect: a straight vertical line was used for the midline so that drawings may be reflected to produce pseudo-bilateral maps of the brain. However the midline of the sections themselves is never perfectly straight, due to small distortions that accompany mounting.

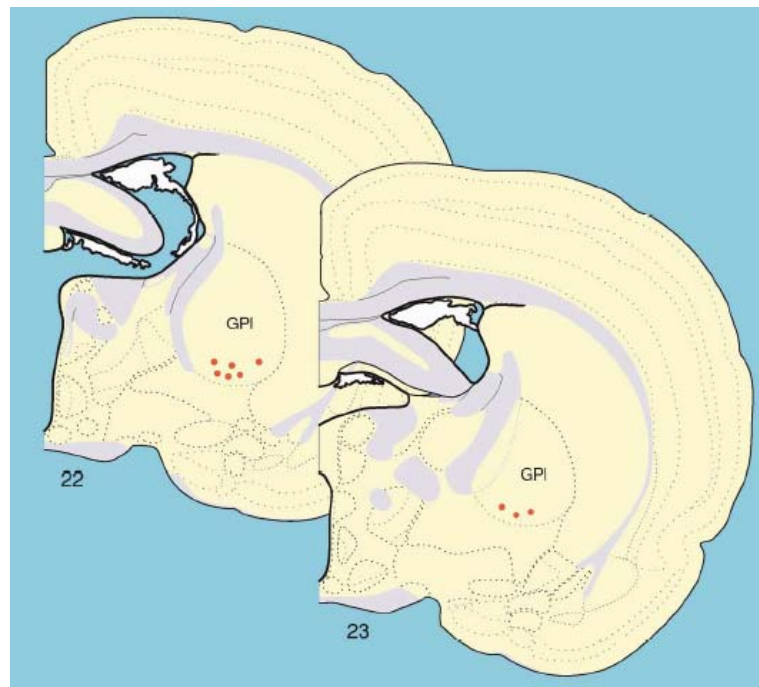


Figure 3.2: Red dots are the reference points that were used to match drawings in different levels of the rat brain [40]

The 73 slices of the atlas were selected out of 556 sections through the brain and each of them has taken about 40 hours of drawing time. The location of these 73 slices

throughout the brain is illustrated in Figure 3.3. Since brain is a very heterogeneous structure, some levels require fewer sections than others for adequate illustration. Each drawing contains a wealthy amount of information regarding the neuroanatomical areas of the brain. Each region which has been identified is also given a label which is the abbreviation of the regions name. There are a total of 1272 labels in the atlas, meaning that one can distinguish 1272 different neuro- and anatomical regions. These labels will serve as the seed points for loop detection in our work. Figure 3.4 shows a small part of section 5 of the brain with the labels.

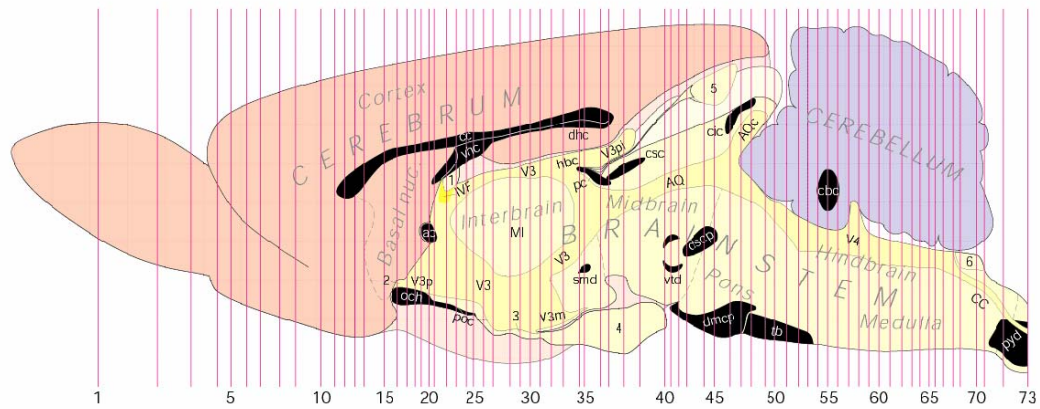


Figure 3.3: Based on complexity of the different brain levels, Swanson has used a variable number of sections per unit length of the brain [40]

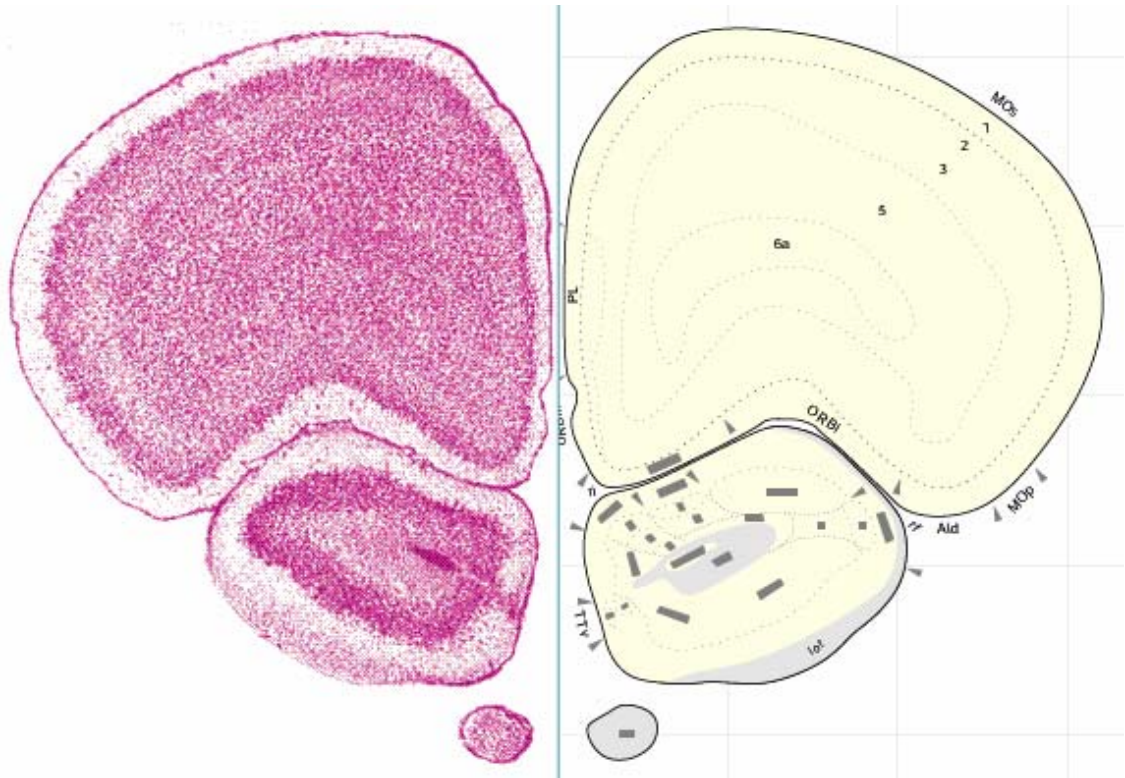


Figure 3.4: Left: Original Nissl-stained brain photomicrographs. Right: Freehand drawing of the brain and delineation of the neuroanatomical region using *AI*TM software [40]

In addition to Swanson's atlas, there are other atlases such as:

1. Paxinos and Watson, 1986
2. DeGroot, 1959
3. König and Klippel, 1963
4. Wüschel et al, 1965
5. Albe-Fessard et al, 1966 and
6. Pellegrino, 1979

3.3 Discrepancies of the atlas

3.3.1 Introduction

A working knowledge of a good computer graphics drawing application (such as *Adobe Illustrator* or *Macromedia Freehand*) is essential for modern rendering and display of structural information. These applications are based on *vector graphics*, which are mathematical descriptions of drawings that have a relatively small file size and can be scaled virtually infinitely without loss of detail. Pixel-based applications are appropriate for the manipulation of digital information (scanned photographs or videophotos), but produce crude drawings and very large file sizes.

There are many advantages of vector graphics over pen and ink drawings. Computer graphics offers the advantage of placing different features of a drawing into separate layers, which are equivalent to a perfectly aligned unlimited stack of transparent overlays. For example, the template for an atlas level can be “dissected” so that cell groups are on the bottom layer, fiber tracts are on the next, the basic outlines of the brain and ventricles are next, and abbreviations are on the top. On the other hand, experience has shown that the time invested in creating good computer graphics drawings pays rich dividends because they (or parts of them copied and pasted) often form the starting point for other drawings, which do not have to be created from scratch. This cloning and modification of existing files is a major advantage of computer graphics over traditional drawing methods.

Despite the aforementioned advantages of the templates and computer drawings, they can be computationally incompatible with existing software and platforms requiring image and graphics information. Also due to inherent characteristics of their creation, which is freehand drawings, they might not comply with strict geometric rules which define the entities represented in the atlases or computer drawings. In the following section, we will address all the issues and the flaws that we encountered in the Swanson's atlas and the next chapter will discuss the measurements that were taken to resolve those issues. The following is the major flaws that were found in the atlas:

1. Multiple lines and curves bundled into a single boundary
2. Non-intersecting or over-extended spline segments
3. Overlapping regions
4. Functional or physical areas labeled remotely from the region
5. Regions without any anatomical label

3.3.2 Multiple lines and curves bundled into a single boundary

Multiple lines and curves bundled into a single boundary was the most common problem in the atlas. *Adobe Illustrator (AI®)* “*preview*” feature masks this redundancy such that the drawing looks as intended. Turning this feature off reveals multiple lines on the boundary of regions which have been created by the drawer when s/he was trying to generate neighboring regions. Figure 3.5 shows an example of such a situation.

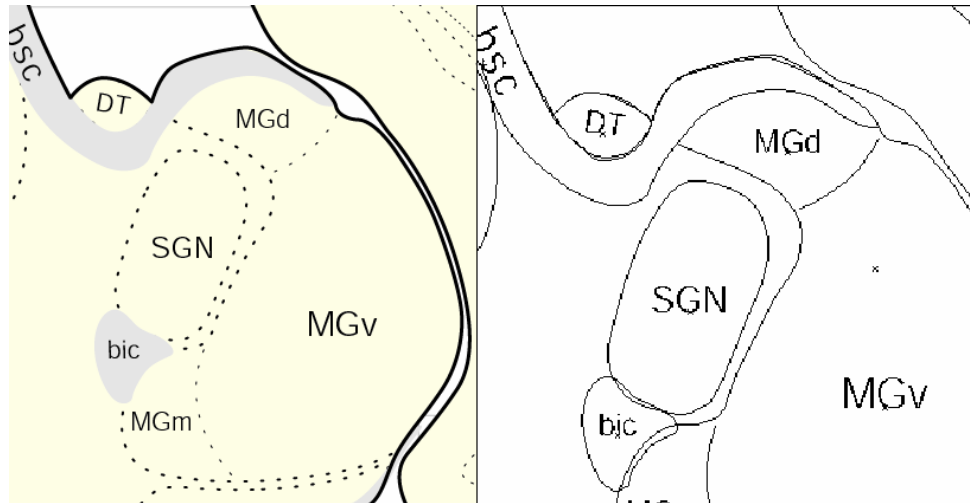


Figure 3.5: Left: A part of a brain map in AI® with preview mode on, Right: same section with preview mode off. Notice the bundled lines and curves in the boundary of the regions

These multiple lines violate the unique definition of each region making the database unsuitable for generation of a 3D database.

3.3.3 Nonintersecting or over-extended spline segments

Numerous situations exist within the atlas drawings where the splines are neither connected nor close to any adjacent geometry entity. This condition makes the delineation of the regions ambiguous. If a bleeding algorithm were used to identify the regions of the brain, these open splines would foil the process. Figure 3.6 shows an example of such a case in the atlas.

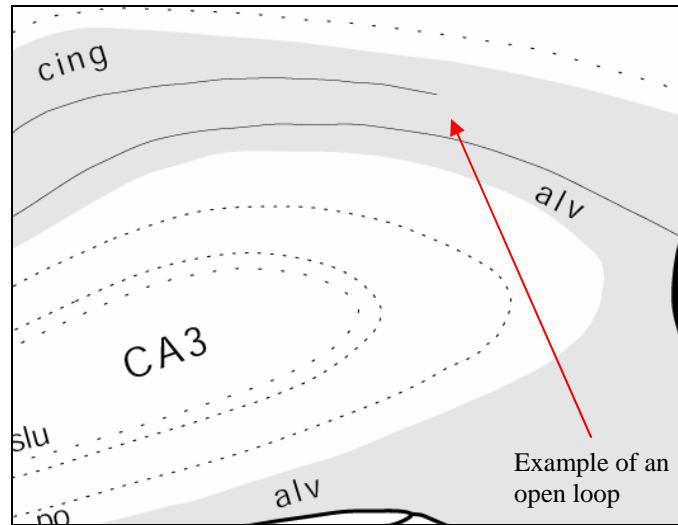


Figure 3.6: An example of un-connected spline in the brain map

3.3.4 Overlapping regions

Since Swanson has used the mask layer feature of *AI*® to generate the drawings, the boundaries of the regions frequently overlap creating ambiguous situations such as in Figure 3.7. In this example a region was created which has no meaning.

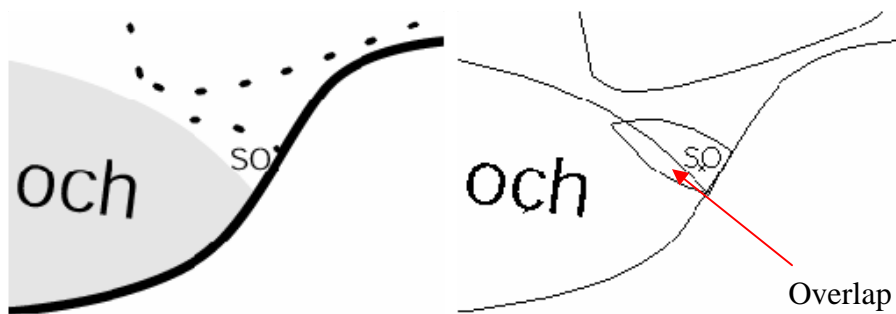


Figure 3.7: Overlapping regions in rat brain atlas

3.3.5 Remotely labeled regions

Some atlas boundary delineations were not intentionally drawn to keep the templates neat and simple looking. An example of such a case is for the areas that control the motion activities of the rat brain. Instead of having the lines inside the drawings, dart-shaped markers were placed on the exterior of the brain to indicate the direction of hypothetical lines, Figure 3.8.

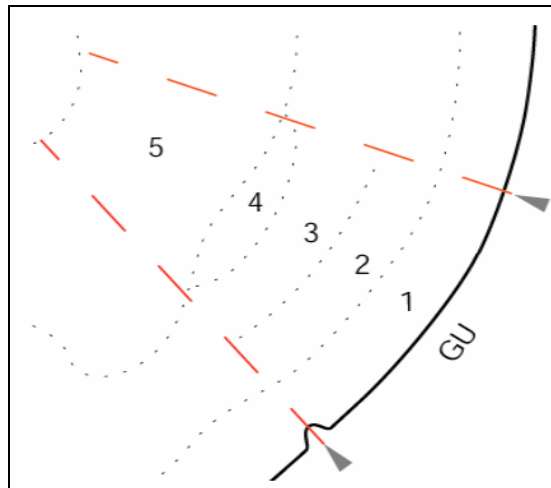


Figure 3.8: Dart-shaped symbols indicate the direction of the boundaries which are supposed to exist (red dashed lines).

3.3.6 Other issues

In addition to the flaws mentioned previously, there are other issues to be addressed. In some slices, abbreviated labels were used for labeling sub-regions of neuroanatomical areas. Obviously these labels do not exist in the label listing of the atlas as they appear on the drawings. For example in level 26, there are labels such as *pmi* or *mpv* which are sub-regions of paraventricular nucleus hypothalamus (*PVH*) and they

should read as: *PVH_{pmi}* and *PVH_{mpv}* in order to show their relevance to the main area.

Also we encountered instances of areas that did not have any labeling although they had a clear boundary curve delineating the region from the background.

Cerebellum lobes within drawings were composed of dotted lines. These lines were not delineations of any anatomical or neuroanatomical regions. Some regions contained multiple labels. The atlas authors did not clearly divide them into sub regions.

4. Algorithms and results

4.1 Introduction

In this section, we discuss the algorithms used to address the issues mentioned in the previous chapter as well as the methods of segmenting the rat brain atlas. These algorithms are presented in the same order that they were implemented within the computer code.

Most atlas curves were in the form of splines¹, therefore to reduce the complexity of the templates; they were approximated by polylines² while maintaining an accurate representation of the original path. All the points were checked to eliminate possible existence of multiple nodes in the same location. Then the polylines were checked for intersection with other polylines. The routines developed merge bundled polylines at boundaries. Thereafter, polylines are merged into loops using a counterclockwise marching line until each loop is closed. Each line segment of the loops separates two materials uniquely. Consequently, each loop has one material common to all line segments which defines the tissue type of the region. Loops with void materials represent overlapping regions or exterior areas and are deleted.

¹ A piecewise polynomial function that can have a locally very simple form, yet at the same time be globally flexible and smooth

² Polylines are series of connected definite lines which may or may not form a close loop.

4.2 Data format

All the drawings are in *Adobe Illustrator*TM file format, which is a proprietary format. Hence, the data was converted to DXF (Drawing eXchange Format), an open data format, for further processing. This DXF format was directly compatible with the *CADKey*TM's CDL file format and was subsequently saved in the CDL ASCII text format. This format stores the mathematical information of the splines, polylines, texts, etc. in readable form. Figure 4.1 shows a sample part of a CDL file.

```
SPLINE C3, SPLTMP, 2, 15, 1, 1, 0, 0, 1, 1
ARRAY SPLTMP[8][12]={0.5470,-0.3586,1.1069,110.5665,-1.092,...}
NNOTE 129.4479, 199.5188, 0.0000, `MOs5`,TXTINFO,TXTATT,ENTATT
ARRAY TXTINFO[6]={0, 0, 1, 0, 0, 2}
LINE 241.0278,124.6897,0.00,206.393,129.4790,0.00,15,1,1,0,0,1,1
```

Figure 4.1: A sample of part of CDL data format

In Figure 4.1, the first line is describing a cubic spline whose coefficients are provided in the next line in the SPLTMP array. The third line is providing the information regarding the label and location of one of the tissues of the brain. And the last line is as an example of a line entity description.

In order to generate a CDL file for each slice of brain, all the drawings files were exported as DXF files and then they were opened in *CADKey*TM software package to create the CDL files.

4.2.1 Splines

When exporting the data into DXF format all the curves in atlas drawings are generated as cubic splines. A cubic spline is a spline constructed of piecewise third-order polynomials which pass through a set of m control points. The second derivative of each polynomial is commonly set to zero at the endpoints, since this provides a boundary condition that completes the system of $m-2$ equations. This produces a so-called "natural" cubic spline and leads to a simple tri-diagonal system which can be solved easily to give the coefficients of the polynomials. However, this choice is not the only one possible, and other boundary conditions can be used instead [41].

Consider 1-dimensional spline for a set of $n+1$ points (y_0, y_1, \dots, y_n) . Let the i^{th} piece of the spline be represented by:

$$y_i(t) = a_i + b_i t + c_i t^2 + d_i t^3 \quad (4-1)$$

where t is a parameter $t \in [0,1]$ and $i = 0, \dots, n$. Then

$$\begin{aligned} y_i(0) &= y_i = a_i \\ y_i(1) &= y_{i+1} = a_i + b_i + c_i + d_i \end{aligned} \quad (4-2)$$

Taking the derivatives of $y_i(t)$ in each interval then give:

$$\begin{aligned} y'_i(0) &= D_i = b_i \\ y'_i(1) &= D_{i+1} = b_i + 2c_i + 3d_i \end{aligned} \quad (4-3)$$

Solving the equations (4-2) and (4-3) for a_i, b_i, c_i and d_i then gives:

$$\begin{aligned}
 a_i &= y_i \\
 b_i &= D_i \\
 c_i &= 3(y_{i+1} - y_i) - 2D_i - D_{i+1} \\
 d_i &= 2(y_i - y_{i+1}) + D_i + D_{i+1}
 \end{aligned} \tag{4-4}$$

Now require that the second derivatives also match at the points, so:

$$\begin{aligned}
 y_{i-1}(1) &= y_i \\
 y'_{i-1}(1) &= y'_i(0) \\
 y_i(0) &= y_i \\
 y''_{i-1} &= y''_i(0)
 \end{aligned} \tag{4-5}$$

as well as that the endpoints satisfy

$$\begin{aligned}
 y_o(0) &= y_0 \\
 y_{n-1} &= y_n
 \end{aligned} \tag{4-6}$$

This gives a total of $4(n-1) + 2 = 4n - 2$ equations for the $4n$ unknowns. To obtain two more conditions, require that the second derivatives at the endpoints be zero, so:

$$\begin{aligned}
 y''_0(0) &= 0 \\
 y''_n(1) &= 0
 \end{aligned} \tag{4-7}$$

Rearranging all these equations (Bartels *et al.* 1998, pp. 12-13) leads to the following beautifully symmetric tri-diagonal system:

$$\begin{bmatrix} 2 & 1 & & & & & \\ 1 & 4 & 1 & & & & \\ & 1 & 4 & 1 & & & \\ & & 1 & 4 & 1 & & \\ \dots & \ddots & \ddots & \ddots & \ddots & \ddots & \ddots \\ & & & 1 & 4 & 1 \\ & & & & 1 & 2 \end{bmatrix} \begin{bmatrix} D_0 \\ D_1 \\ D_2 \\ D_3 \\ \vdots \\ D_{n-1} \\ D_n \end{bmatrix} = \begin{bmatrix} 3(x_1 - x_0) \\ 3(x_2 - x_0) \\ 3(x_3 - x_1) \\ \vdots \\ 3(x_{n-1} - x_{n-3}) \\ 3(x_n - x_{n-2}) \\ 3(x_n - x_{n-1}) \end{bmatrix} \quad (4-8)$$

By solving the equation (4-8), one can solve for the 3rd degree polynomial coefficients.

4.3 Manual Modifications

There were some inevitable manual modifications required before automatic processing of flaws in the atlas. Lines were created within the atlas associated with the dart-shaped markers, described in section 3.3.5. Also, due to lack of space in some small areas of the brain, atlas labels were placed outside those regions. We manually decreased the size of the font and moved the label into corresponding zone. We also exploited the symmetry of the brain maps and just used the right half of the brain, this reduced the time of the computation drastically.

A small thumbnail of a coronal sagittal view existed on the upper right corner of each map to show the location of each section on longitudinal axis of the brain. This thumbnail was also deleted. We left the dart-shaped markers intact because they would be detected and expunged by our algorithms.

4.4 Automatic Modifications

This section describes how the algorithms handled various problems in the drawings. Also the methods that were used to identify each region and assign the appropriate tissue labels are delineated.

4.4.1 Spline Approximation

The dominant drawing entities are splines. To reduce the complexity of calculations, and hence the CPU usage time, they were approximated by polylines. Each segment of the spline was replaced with 4 straight lines. To demonstrate this better, in equation (4-9) if we just give the spline parameter, i.e. t , start and ending values, the spline will be presented by a single line, as in Figure 4.2:

$$\begin{aligned}x_i &= ax_i \cdot t^3 + bx_i \cdot t^2 + cx_i \cdot t + dx_i \\y_i &= ay_i \cdot t^3 + by_i \cdot t^2 + cy_i \cdot t + dy_i\end{aligned}\tag{4-9}$$



Figure 4.2: Spline Approximation. Red curve is the spline which has been roughly approximated by assuming just two values of 0 and 1 as for its parameter

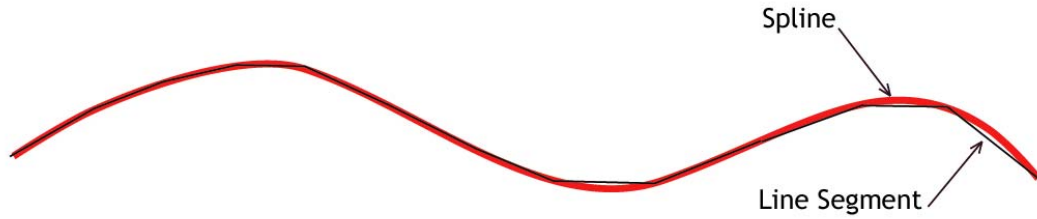


Figure 4.3: The same spline approximated with for line segments, corresponding to t values of 0, 0.25, 0.75 and 1.

The routine that reads the splines, handles the approximation by using four values for t : 0, 0.25, 0.75 and 1 (Figure 4.3). The maximum error incurred was less than $\frac{1}{4}$ of a percent (0.0025). This insignificant error was associated with area shrinkage for splines with drastically changing curvatures (for example for splines depicting the choroids plexus (CHP) in section 25 of the brain).

After this step, all overlapping nodes are merged. The lineal span was less than 3×10^{-8} of the box width enclosing the brain map.

4.4.2 Extend/Intersect/Merge

The term “*Node*” refers to endpoints of each line segment and “*Element*” is used for the lines connecting the nodes. Note that all the data extracted from *AI*TM files, including splines, lines, and conic sections are now represented/approximated by a finite number of lines. Therefore our database of atlas drawings consists of nodes and their coordinates and the connectivity of those nodes defined by the elements.

Open loops are identified by nodes attached to only *one* element. The algorithm follows:

Do Loop until the last node, i
 *If **node_i** exists in at least at 2 elements,*
 Continue loop i;
 Else
 Find the shortest normal distance from the node_i to adjacent
 elements and save the element number: element_j
 *If **node_i** lies within the **element_j** box,*
 *Snap **node_i** into **element_j***
 Else
 *Connect **node_i** to the closest node of **element_j***
 End Loop

The 2 different situation of connecting an open node to an element or another node is depicted in Figure 4.4.

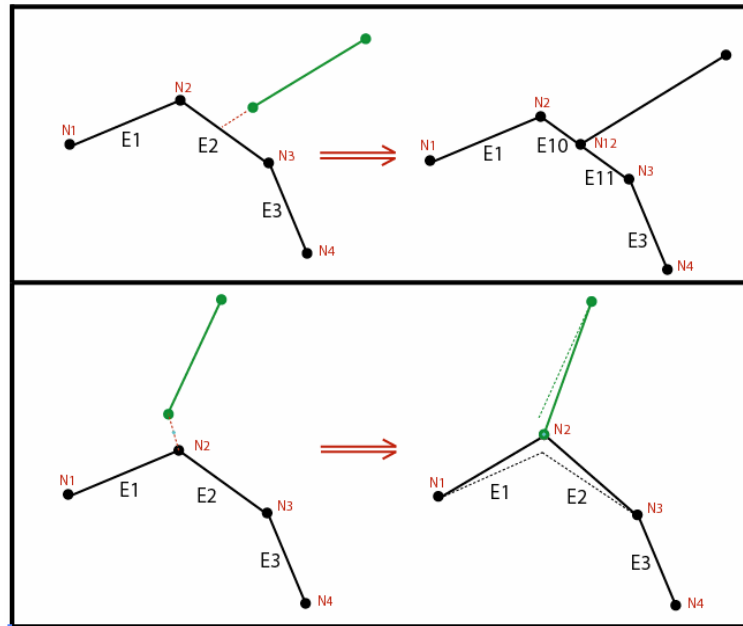


Figure 4.4: Above: Open node lies in the $E2$ element box, thus it is snapped into element.
 Below: Open node is outside the box, so it is directly connected to endpoint of the $E2$

New nodes were created whenever two elements intersected. This step was necessary because our algorithms assume that all elements separate two distinct materials only. Consequently, any intersecting elements are converted into 4 elements with the new node common to all. This guarantees a consistent topographic map of elements and nodes. This concept can be expressed as:

$$\text{if } x \in A \cap B \Rightarrow x \in A1 \cup B1,$$

where,

A : Set of points belonging to element 1

B : Set of points belonging to element 2

$A1$: Endpoint nodes of A , $n(A) = 2$

$B1$: Endpoint nodes of B , $n(B) = 2$

The same applies for elements, i.e. there can't exist two elements connecting the same two nodes, therefore:

$$A \subseteq B \Rightarrow A = B, \text{ or}$$

$$\text{if } n(A \cap B) > 1 \Rightarrow A = B$$

Thus we also merged redundant elements, Figure 4.5.

4.4.3 Identify brain regions

In this step, the code categorizes elements to define regions corresponding to different areas of the brain. The text labels, provided in each brain map, were used as seed point locations. There were 1272 labels identifying the various neuroanatomical

areas of the brain. Each element will assume two new features in addition to its nodes: material code *A* and *B* which have been separated by the element.

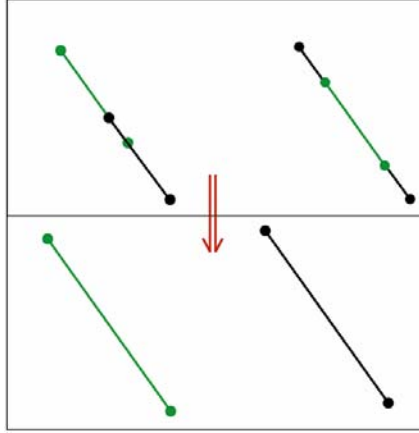


Figure 4.5: Merging redundant elements

In order to determine tissue codes for each element, the coordinates of the seed points (atlas text labels) were used. A temporary semi-finite line was added to our nodes and elements database whose start point coordinate was the same as the seed point and its direction was completely arbitrary. Then all the elements intersected by this newly introduced line were tagged as potential elements belonging to tissue type in question. In order to narrow down to just one element, the tagged elements were sorted based on their distance to the seed point and the closest one was chosen as the element delineating the boundary of tissue *A* of the brain. Now one can legitimately assume that there exists at least one element attached to the recently found element which is also part of the boundary of tissue *A*. If there exist more than one attached element, then the elements will be selected whose cross product with the current one results in a positive vector, in another word, using this method we choose the most left element connected to current

one. 'Left' is defined as the left hand side of an imaginary observer who is walking on the trail of current element from its tail to its head. Now that a new element of tissue type A has been identified, the algorithm will continue to find next legitimate attached element. This process will continue till we find all the elements forming a closed loop around that specific tissue type of the brain. We will refer to this process as a counter clockwise marching line algorithm, Figure 4.7.

This algorithm can be expressed as:

Shoot a semi-infinite line and collect the intersected elements

Find the closest intersected element to the seed point and take it as the starting element

Do Loop until current elements becomes start element

Proceed to the next element based on a tail-to-head logic

If the current head node is shared by more than one element, select the element based on right-hand rule, i.e. steer to the relative left element

Keep the current element information in an array

End Loop

If the number of shared elements between the current loop and elements in global array of intersected is even

Repeat the above loop

Else

Assign the tissue code of the current seed point to the elements of the already recognized loop.

This algorithm can be used for all the seed points in the current map, but it does not guarantee that all the elements within our database have been completely classified. There can be instances that some elements would only have one tissue code assigned to

them because they were located in the map such that they were close to only one seed point, i.e. they have been crossed only once by imaginary semi-infinite lines. Thus the second ID code for the loop elements is unknown.

As shown in Figure 4.8, the elements of region denoted by label “*PS*” could not be seen by other seed points except for “*PS*”. In order to resolve this issue we first need to identify those elements in our database. Then a simple, yet very efficient and robust, method was used to figure out the second ID [42]. The following is the description of the method (see Figure 4.6).

- ii) Create a semi-infinite line starting at midpoint of the element with one material ID
- iii) Determine the intersection of line with all elements of the database. Let

$S = \{\overrightarrow{P_i Q_i}, i = 1, N\}$ be the set of line segments representing the region boundaries, and $y = H$ be the equation of the horizontal line. The intersection points between the given horizontal line and the region are determined by considering the line segments of S one by one. Consider line segment $\overrightarrow{P_i Q_i}$ as an example.

Write $X_1 = X(P_i), Y_1 = Y(P_i), X_2 = X(Q_i), Y_2 = Y(Q_i)$. There is intersection if

- a) $(Y_1 - H)(Y_2 - H) < 0$ or
- b) $(Y_1 - H)(Y_2 - H) = 0$ and $(H > Y_1 \text{ or } H > Y_2)$

For any other cases, it is considered that there is no intersection. The point of

intersection is given by:

$$\left(X_1 + \frac{(H - Y_1)(X_2 - X_1)}{(Y_2 - Y_1)}, H \right)$$

- iv) The intersection points are arranged in ascending magnitude of X
- v) Find the region codes present in the intersection list and count the number of each code.

The region ID whose occurrence count in intersection list is odd will be our missing code for the isolated loop (Figure 4.8)

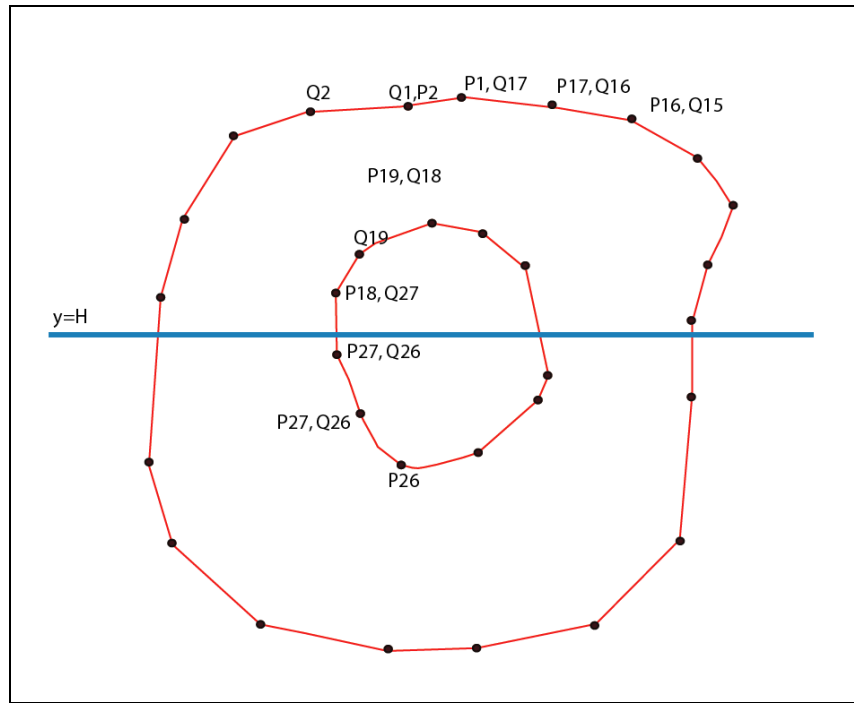


Figure 4.6: Line crossing algorithm to identify regions defined by line segments

This can be shown as following algorithm:

— Identify the elements with only one material code

- Shoot a semi-infinite line from midpoint of the element and collect the intersected elements
- Count the number of occurrence of each material in the intersected element list
- Pick the material code which has the odd number of occurrences and assign it to the elements of the current loop.

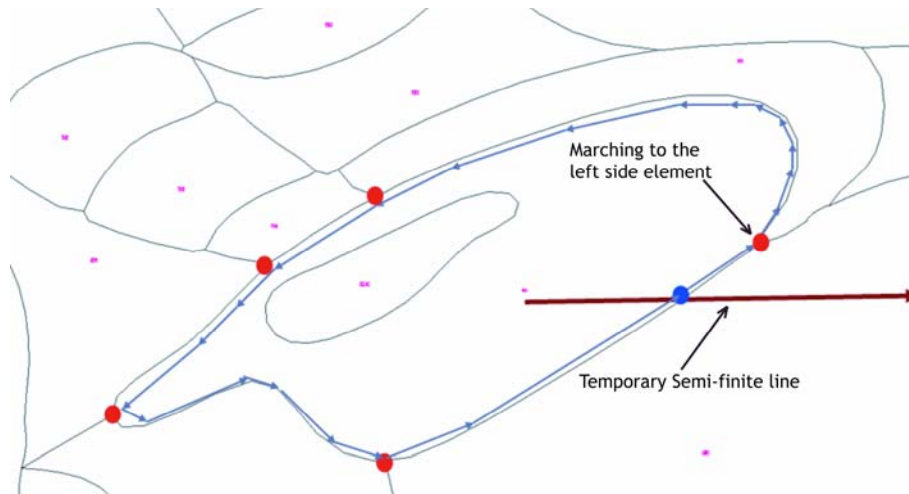


Figure 4.7: Using seed points to identify regions of the brain and assigning material codes to the defining boundary elements.

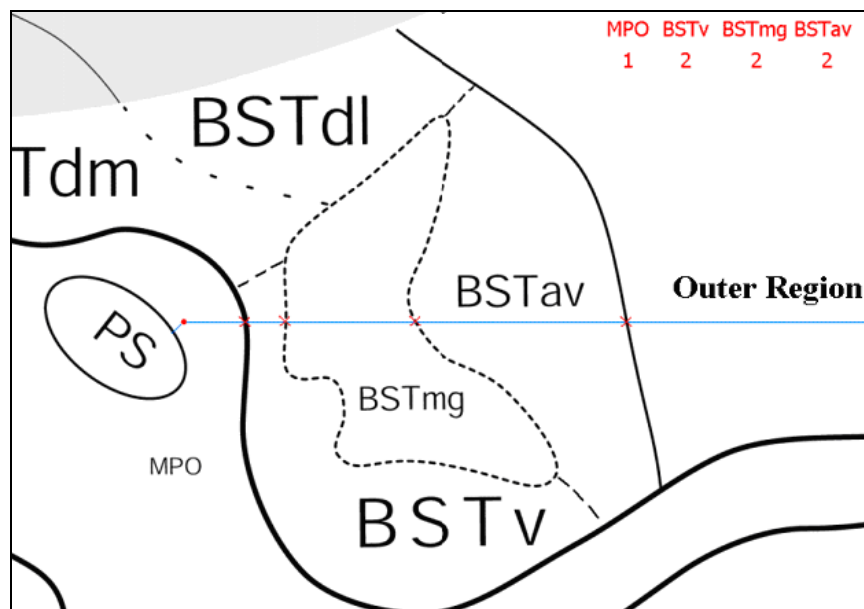


Figure 4.8: Finding the isolated islands and figuring out the second material code

4.4.4 Overlapping areas

When boundary definitions overlap void regions are created which need to be zippered. Elements adjacent to these void regions are missing one of the material attributes and can be identified easily. The void region is zippered by calculating midline locations between opposing boundaries as shown in Figure 4.9.

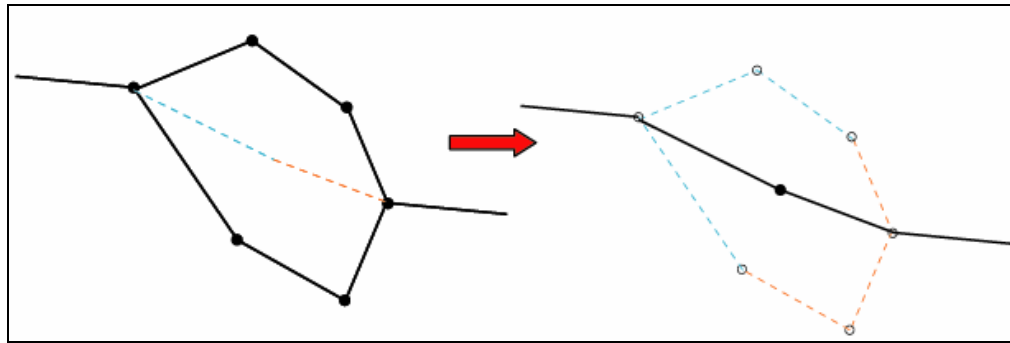


Figure 4.9: Removing the void loops whose elements have just one material code

4.4.5 Mirroring and output

After all elements are identified and assigned to appropriate loops, a routine re-sequences the node and element numbers prior to output. The atlas took advantage of symmetry and created only the left half. We mirrored the nodes and elements along the Superior-Inferior midline to create the full brain image.

The code outputs in ASCII format a text file containing the node numbers and their coordinates as well as the elements and their four attributes (two node numbers and two material codes).

4.5 The code

The algorithms were implemented using C++ language. The code is strictly in compliance with ANSI C++ standard and it uses standard libraries of C++ which makes it a cross-platform piece of software. Therefore we were able to successfully compile and run the code in following operating systems:

1. Microsoft Windows
2. 2 different versions of UNIX (SGI[®] and Sun Microsystems[®])
3. Linux (Red Hat 9.0 distribution)

It is possible to process the whole or some sections of the brain in one execution of the program. With minor modifications of the code, it can be used to process other brain atlases such as mouse and human. The program contains approximately 3000 lines of code.

4.6 Results

The output files delineate each material region uniquely. They are suitable for further numerical analyses such as the work presented in [42]. To visualize the output of the code, a utility was developed to convert the results into a Microsoft Windows “.bmp” image. Figure 4.10 shows the result for section 26 of the rat brain.

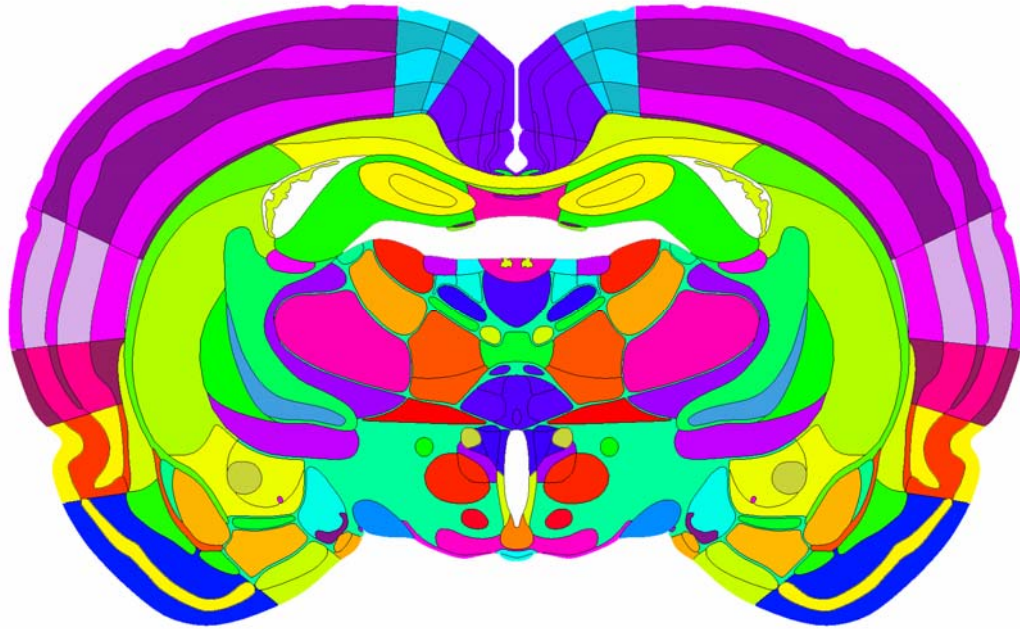


Figure 4.10: Level 26 of the rat brain after segmentation. Each colored area is defined with unique nodes and elements.

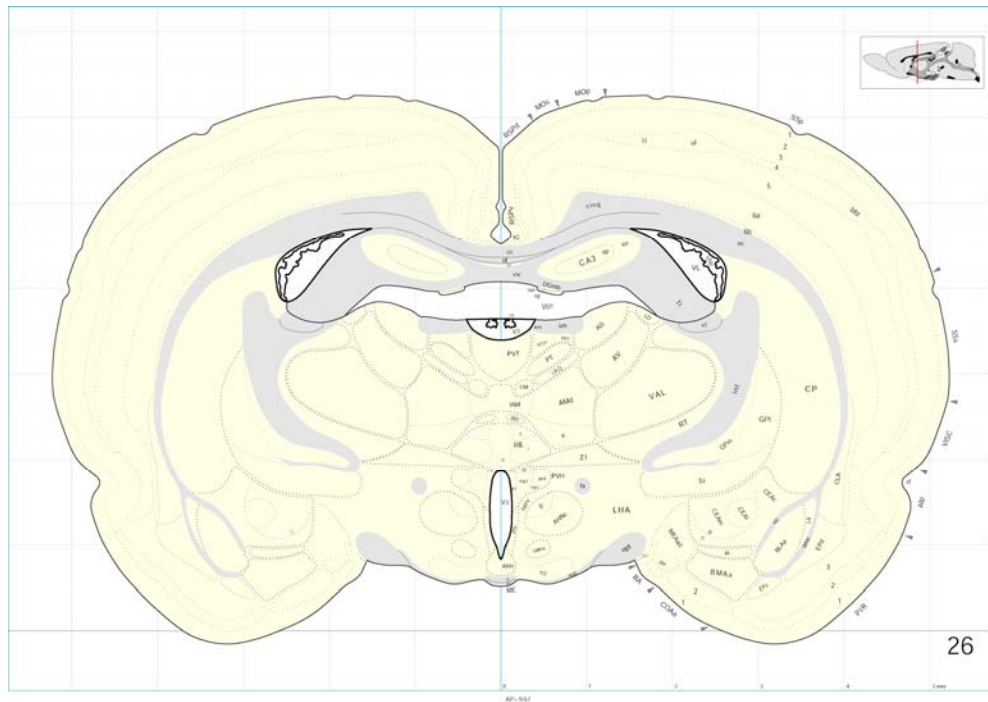


Figure 4.11: AT™ drawing of level 26. As mentioned before, these files have flaws and discrepancies, so they cannot be considered numerically suitable data

Also Figure 4.12 shows another sample of the result. After running the code, the output was taken into *GMS*[®] software in which for each region a colorful mesh is generated. Then the original *Adobe*[®] *Illustrators*[®] file is superposed on top of the generated meshes. Two files show a perfect match between the original files and the code's output. The indented mismatch at some of the boundaries is due to resolution of the mesh.

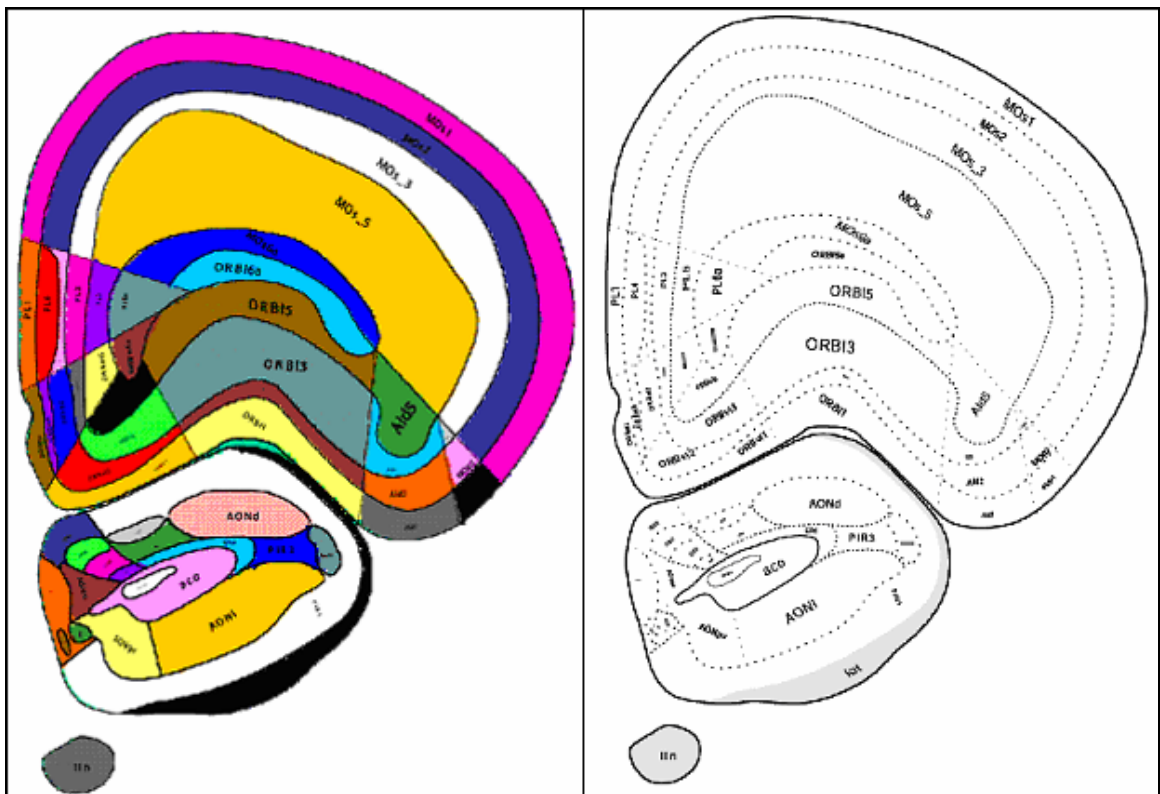


Figure 4.12: Superposition of the results on the original drawing file. Left: the results were taken to *GMS*TM software and area mesh was generated for each region. Right: the original *AI*TM file

Kulkarni et al [42] used the results of this work and reconstructed 3D model of all 1272 parts of the brain as well as the brain cortex via a multiple-material marching cube. Figure 4.13 shows a sample of their result.

Similarly, the multiple material marching cube algorithm [47] was applied to different functional parts of the rat brain to create functional sub-volumes. Those segmented volumes of brain were used to register the result of a functional MRI study in which the brain activity of a lactating dam was studied during different stimuli [46].

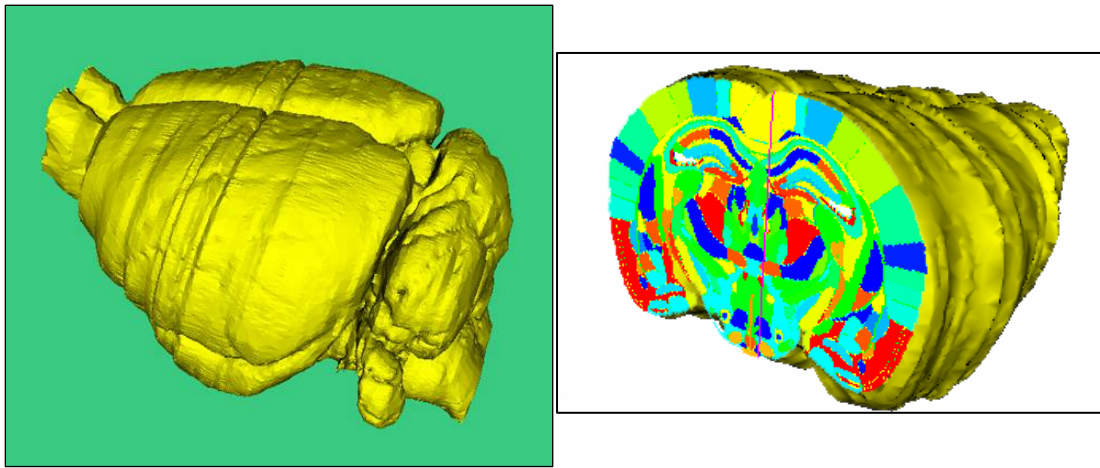


Figure 4.13: A 3D model of the Sprague-Dawley rat brain reconstructed from 2D data resulted from this work [42]

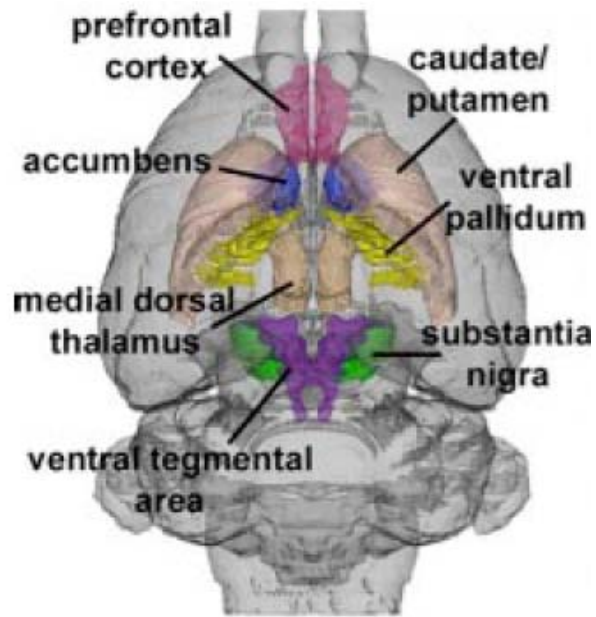


Figure 14: Volume Segmentation: 3D extrapolation of 2D slices and classification of the functional regions of brain [46]

The following flowchart gives a general idea about how this work can be combined with other image analysis to form a complete medical image application.

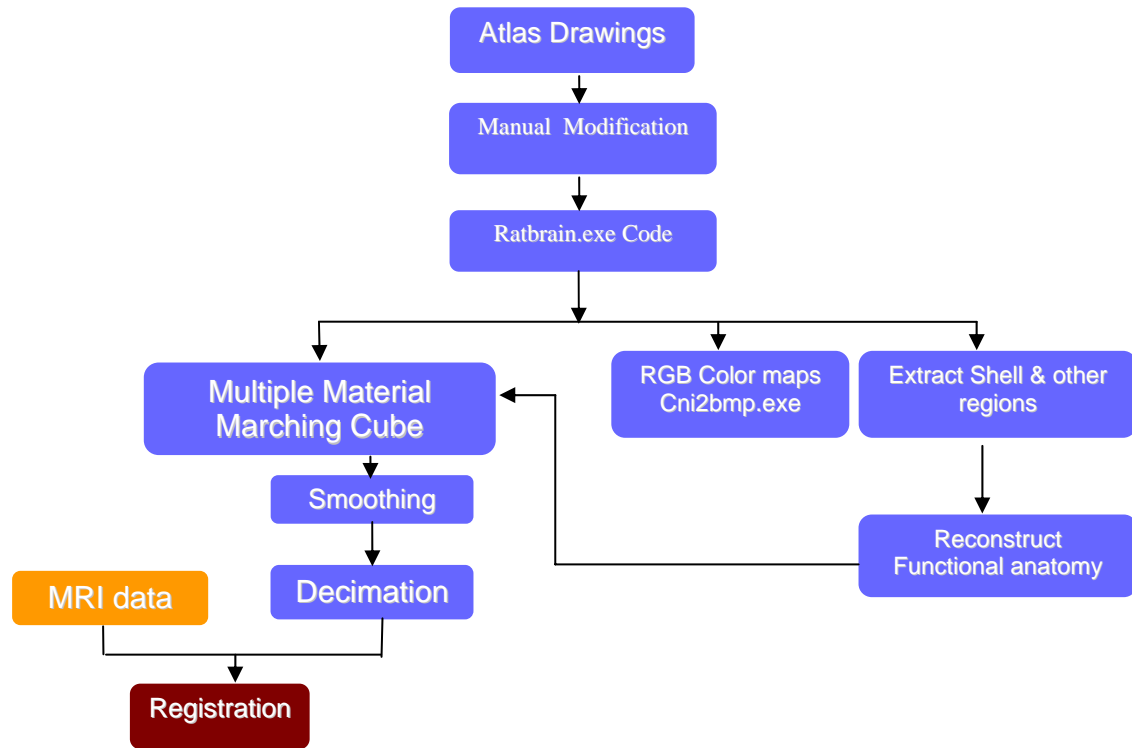


Figure 4.15: Flowchart of the work that can be accomplished using the results of this work

4.7 Conclusions

Atlases are a primary source of information for studying the brain. A common approach to segment an image dataset is to use a standard atlas to identify different regions of interests. Algorithms for a semi-automatic segmentation of 2D slices of a rat brain atlas have been developed and implemented in this work. Swanson's Rat Brain Atlas, which is a gold standard atlas in neuroanatomical studies, was chosen as the feed for the algorithms. This atlas provides freehand drawings of 73 slices through a Sprague-

Dawley rat brain. The data are provided in a vector graphic format which is suitable for conversion to DXF format for further numerical processing.

Although this atlas provides information about 1200 different regions of the brain, the drawings are not numerically robust, making them unusable for numerical computation or solid model reconstruction. These inconsistencies prevent a straightforward segmentation process. Hence, a variety of tools were designed and applied to address these issues. The result was the creation of a database of boundary elements and nodes which are numerically robust and consistent. These boundaries delineate regions and tissues of the brain facilitating the creation of a fully segmented atlas suitable for further processing, including 3D reconstruction and numerical analysis.

The anomalies found in the atlas were classified as: multiple definitions of ROI boundaries, non-intersecting or over-extended spline segments, overlapping regions, extra markers or labels remotely placed in the drawings and extra boundary lines within the same functional or physical area. Each slice of the atlas was parsed through an ASCII file in DXF format. For each slice, the information of splines (curves defining boundaries), labels and their location were extracted. Splines were replaced with polyline segments to reduce the size and complexity of the data while maintaining accurate shapes of the original curves. Each line was considered an element which contains two nodes, their coordinates, and connectivity information. All elements in the current slice were examined for intersections with other elements. In case of an intersection, the routine either trimmed the element or split it into two new ones by introducing a new node.

Subsequently, seed points resident in the dataset were used to classify regions into closed loops using a counterclockwise path. Each element was assigned two material codes identifying the two regions it separated. All members of each loop have one material code in common which is that of the enclosed tissue or neurological area of the brain.

At the end, for each slice a file, containing all the loops, nodes and element information, was created which was used as input for other routines, such as the marching cube algorithm to reconstruct a 3D brain.

5. References

- [1]. Preston, K. Jr., Taylor, J.W.K, *Medical Imaging Techniques, A Comparison*, Plenum Press, New York, 1979.
- [2]. W.K. Röntgen (transl. by A. Stanton), *On a new kind of rays*, Nature 53:274-276, January 1896.
- [3]. G.N. Hounsfield, *Potential uses of more accurate CT absorption values by filtering*, AJR 131:103, 1978
- [4]. A.M. Cormack, *Representation of a function by its line integrals, with some radiological applications*, J. App. Physics 34:2722-2727, 1963
- [5]. Clarke, L.P.; Velthuizen, R.P.; et al., *MRI Segmentation and Applications*, Magnetic Resonance Imaging, Vol. 13, No. 3, pp. 343-368, 1995
- [6]. MRI Artifact Gallery, <http://bmrl.med.uiuc.edu/mriartgallery/>
- [7]. *CT Image Quality*, http://www.t2star.com/CT_IQ/CT_IQ.pdf
- [8]. Plante, E.; Turkstra, L.; *Sources of error in the quantitative analysis of MRI scans*, Magnetic Resonance Imaging 9:589-595, 1991
- [9]. Jain, A.K.; *Fundamentals of digital image processing*, Englewood Cliffs, NJ: Prentice Hall, 1989
- [10]. Ashtari, M.; Zito, J.L.; et al; *Computerized measurement of brain structure*, Invest. Radiology 25:798-805, 1990
- [11]. Waks, H.H; Teritiak, O.J.; *Recognition of regions in brain section*, Computational Medical Imaging Graphics 14:341-352, 1990

- [12]. Canny, J.; *A computational approach to edge detection*, IEEE Trans. Patt. Anal. and Machine Intell. 8:679-698, 1986
- [13]. Raff, U.; Newman, F.D.; *Automated lesion detection and lesion quantitation in MR images using auto-associative memory*, Med. Phys. 19:71-77, 1992
- [14]. Ehrlicke, H.H.; *Problems and approaches for tissue segmentation in 3D MR imaging*, In: M.H. Loew (Ed.) Medical Imaging IV: Image Processing. Proceedings SPIE 1233L128-137, 1990
- [15]. Schad, L.R.; Bluml, S.; Zuna, I.; *MR tissue characterization of intracranial tumors by means of texture analysis*, Magn. Reson. Imaging 11(6):889-896, 1993
- [16]. Analyze Direct, comprehensive visualization for biomedical imaging,
<http://www.analyzedirect.com/>
- [17]. Suzuki, H.; Toriwaki, J.; *Automatic Segmentation of Head MRI Images by Knowledge Guided Thresholding*, Comp. Med. Imaging Phys. 15:233, 1991
- [18]. Gregoire, M.; *Edge Detection*, <http://www.sop.inria.fr/epidaure/personnel/malandain/segment/edges.html>
- [19]. Bezdek, J.C.; Hall, L.O.; et al; *Review of MR image segmentation using pattern recognition*, Med. Phys. 20:1033-1048, 1993
- [20]. Clarke, L.P; Velthuizen, R.P.; et al; *Stability of three supervised segmentation techniques*, Magn. Reson. Imaging 11:95-106, 1993
- [21]. Gerig, G.; Martin, J.; Kikinis, R.; et al; *Unsupervised tissue segmentation of 3D dual-echo MR head data*. Image Vision Computer 10:349-360, 1992

- [22]. Agartz, I.; Saaf, J.; Wahlund, L.; Wetterberg, L.; *Quantitative Estimations of Cerebrospinal Fluid Spaces and Brain Regions in Healthy Controls Using Computer-Assisted Tissue Classification of Magnetic Resonance Images: Relation to Age and Sex*, Magn. Reson. Imaging 10:217-226, 1992
- [23]. Strzecha, K.; *Image segmentation algorithm based on statistical pattern recognition methods*, Exper. Design Appl. CAD in Microelec., Proceedings of 6th Int. Conf., 2001
- [24]. Jasjit, S.S.; Sameer S.; Laura R.; *Computer Vision and Pattern Recognition Techniques for 2-D and 3-D MR Cerebral Cortical Segmentation (Part I): A State-of-the-Art Review*, Pattern Analysis and applications 5:77-98, 2002
- [25]. Cover, T.M.; Hart, P.E.; *Nearest Neighbor Pattern Classification*, IEEE transactions on Information Theory, Vol. 13, No. 1, 1967
- [26]. Warfield, S.; *Fast k-NN classification for multichannel image data*, Pattern Recognition Letters 17:713-721, 1996
- [27]. Dubes, R.; Jain, A.; *Algorithms that Cluster Data*, Englewood Cliffs, NJ: Prentice Hall, 1988
- [28]. Bishop, C.M.; *Neural Networks for Pattern Recognition*, Clarendon Press, Oxford, 1995.
- [29]. Bezdek, J.C.; *Pattern Recognition with Fuzzy Objective Function Algorithms*, Plenum, New York, 1981
- [30]. Zadeh, L.A.; *Fuzzy Sets*, Information and Control, 8:338-353, 1965

- [31]. Cho, Z.H.; *Special Issue on Physical and computational aspects of 3D image reconstruction*, IEEE Trans. Nucl. Sci., NS21, 1974
- [32]. Cho, Z.H.; *Foundations of Medical Imaging*, John Wiley and Sons, New York, 1993
- [33]. Remote Sensing Tutorial, http://rst.gsfc.nasa.gov/Intro/Part2_26c.html
- [34]. MEDx, multi-modality medical image analysis software, <http://medx.sensor.com/products/medx/overview.html>
- [35]. Analyze, <http://www.mayo.edu/bir/Software/Analyze/Analyze.html>
- [36]. Insight Segmentation and Registration Tool, <http://www.itk.org/>
- [37]. IDL Software, <http://www.rsinc.com/idl/>
- [38]. MVTech Halcon, <http://www.mvtec.com/halcon/>
- [39]. Clark, M.C; Hall, L.O.; Goldgof, D.B.; et al; *MRI segmentation using fuzzy clustering techniques: Integrating Knowledge*, IEEE Engin. Med. Biol. 13(5):730-742, 1994.
- [40]. Swanson, L.W.; *Brain Maps: Structure of the Rat Brain*, Second Edition, Elsevier, 1998
- [41]. Cubic Spline, <http://mathworld.wolfram.com/CubicSpline.html>
- [42]. Kulkarni, P.P.; Sullivan, J.M.; Ghadyani, H.R.; Huang, W.; Wu, Z.; King, A.; *Automatic Segmentation of a Rat Brain Atlas via a Multiple-Material Marching Cube Strategy*, Proc. Intl. Soc. Mag. Reson. Med. 11(2003), Canada
- [43]. Lo, S.H.; *A New Mesh Generation Scheme For Arbitrary Planar Domains*, Intl Journal for Num. Methods in Eng., Vol 21, 1403-1426, 1985

- [44]. Bondiau, P.Y.; Malandain, G.; *Atlas-based automatic segmentation of MR images: Validation study on the brainstem in radiotherapy*, International Journal of Radiation Oncology Biology Physics 61(1):289-298, 2005
- [45]. Kikinis, R; Shenton, M.E.; *A digital brain atlas for surgical planning, model-driven segmentation, and teaching*, IEEE Trans on Visualization and Computer Graphics, 2 (3): 232-241 SEP 1996
- [46]. Ferris, C.F.; Kulkarni, P.; Sullivan, J.M.; *Pup Suckling Is More Rewarding Than Cocaine: Evidence from Functional Magnetic Resonance Imaging and Three-Dimensional Computational Analysis*, The Journal of Neuroscience, 25(1):149 – 156, Jan 2005
- [47]. Wu, Ziji; Sullivan, John M., Jr.; *Multiple material marching cubes algorithm*, International Journal for Numerical Methods in Engineering, 58(2):189-207, July 2003
- [48]. Remote Sensing Tutorial Introduction,
http://rst.gsfc.nasa.gov/Intro/Part2_26c.html
- [49]. Comaniciu, D.; P. Mere; *Robust Analysis of Feature Spaces: Color Image Segmentation*, Proc. IEEE Computer Vision and Pattern Recognition, 750-755, June 1997
- [50]. Peng, Y; *CT/PET Fusion Multi-modal visualization of PET and CT volume data to define target volumes in radio-oncology*, <http://a7www.igd.fhg.de/images-video/fusion/fusion.html>

- [51]. Imaging Science at RIT, <http://www.cis.rit.edu/htbooks/mri/chap-14/chap-14.htm#14.1>
- [52]. Functional Basics of CT, <http://imagnis.com/graphics/ct-scan/>